

Binary neutron star populations in the Milky Way

Cecilia Sgalletta^{1,2*}, Giuliano Iorio^{2,3†}, Michela Mapelli^{2,3,4‡}, M. Celeste Artale^{2,3,5}, Lumen Boco¹,
 Debatri Chattopadhyay⁶, Andrea Lapi¹, Andrea Possenti⁷, Stefano Rinaldi^{8,9}, Mario Spera^{1,10}

¹SISSA, via Bonomea 365, I-34136 Trieste, Italy

²INFN-Padova, Via Marzolo 8, I-35131 Padova, Italy

³Dipartimento di Fisica e Astronomia Galileo Galilei, Università di Padova, Vicolo dell'Osservatorio 3, I-35122 Padova, Italy

⁴INAF-Padova, Vicolo dell'Osservatorio 5, I-35122 Padova, Italy

⁵Departamento de Ciencias Físicas, Universidad Andres Bello, Fernandez Concha 700, Las Condes, Santiago, Chile

⁶Gravity Exploration Institute, School of Physics and Astronomy, Cardiff University, Cardiff CF24 3AA, UK

⁷INAF-Osservatorio Astronomico di Cagliari, Via della Scienza 5, I-09047 Selargius, CA, Italy

⁸Dipartimento di Fisica “E. Fermi”, Università di Pisa, I-56127 Pisa, Italy

⁹INFN, Sezione di Pisa, I-56127 Pisa, Italy

¹⁰National Institute for Nuclear Physics - INFN, Sezione di Trieste, I-34127 Trieste, Italy

Accepted XXX. Received YYY; in original form ZZZ

ABSTRACT

Galactic binary neutron stars (BNSs) are a unique laboratory to probe the evolution of BNSs and their progenitors. Here, we use a new version of the population synthesis code `SEVN` to evolve the population of Galactic BNSs, by modeling the spin up and down of pulsars self-consistently. We analyze the merger rate \mathcal{R}_{MW} , orbital period P_{orb} , eccentricity e , spin period P , and spin period derivative \dot{P} of the BNS population. Values of the common envelope parameter $\alpha = 1 - 3$ and an accurate model of the Milky Way star formation history best reproduce the BNS merger rate in our Galaxy ($\mathcal{R}_{\text{MW}} \approx 30 \text{ Myr}^{-1}$). We apply radio-selection effects to our simulated BNSs and compare them to the observed population. Using a Dirichlet process Gaussian mixture method, we evaluate the four-dimensional likelihood in the $(P_{\text{orb}}, e, P, \dot{P})$ space, by comparing our radio-selected simulated pulsars against Galactic BNSs. Our analysis favours an uniform initial distribution for both the magnetic field (10^{10-13} G) and the spin period (10 – 100 ms). The implementation of radio selection effects is critical to match not only the spin period and period derivative, but also the orbital period and eccentricity of Galactic BNSs. According to our fiducial model, the Square Kilometre Array will detect ~ 20 new BNSs in the Milky Way.

Key words: stars: neutron – gravitational waves – binaries: general – pulsars: general – methods: numerical

1 INTRODUCTION

Radio pulsars are highly magnetized, rapidly spinning neutron stars (NSs) that emit beams of electromagnetic radiation, making them some of the most precise cosmic clocks known to science (Hewish et al. 1968; Pacini 1968). They can provide us with a wealth of information. Their spin period and spin period derivative can be measured with high accuracy. The timing precision of radio pulsars allows for tests of general relativity in the strong-field regime, which would otherwise be unfeasible with terrestrial laboratories. The only binary pulsar system known to date, PSR J0737-3039A/B (Burgay et al. 2003; Lyne et al. 2004), is a unique laboratory for tests of gravity theories and for the study of highly condensed matter (e.g., Kramer et al. 2006; Lattimer 2021). Moreover, the pulsar timing array (PTA, a set of pulsars which is analysed to search for correlated signatures in the pulse arrival times Hobbs et al. 2010; Hobbs 2013; Manchester et al. 2013; Lentati et al. 2015; Arzoumanian et al. 2018; Miles et al. 2023) makes it possible to investigate the sources of low-frequency

gravitational waves (GWs), such as super-massive black hole mergers (Arzoumanian et al. 2020).

The formation and evolution properties of pulsars are still matter of debate. Earlier efforts attempted to infer the birth distribution of pulsar properties from their observed Galactic population (Ostriker & Gunn 1969; Faucher-Giguère & Kaspi 2006), the main long-standing issue being that of magnetic field decay (Faucher-Giguère & Kaspi 2006). Based on a theoretical argument, magnetic field decay might generate from Ohmic dissipation, caused by the formation of electric currents on the NS crust (Bhattacharya et al. 1992; Konar & Bhattacharya 1997, 1999). This effect is probably more relevant, however, during accretion (Kiel et al. 2008). A number of magnetic field decay timescales has been explored to date (Gonthier et al. 2004; Faucher-Giguère & Kaspi 2006; Kiel et al. 2008; Osłowski et al. 2011; Chattopadhyay et al. 2020, 2021). The understanding of pulsars birth properties might help to shed light on the supernova (SN) explosion mechanism, because we expect that the newly-born NS properties are tightly correlated with the pre-SN star (Faucher-Giguère & Kaspi 2006; Kapil et al. 2023).

The presence of a radio pulsar in a binary system allows us to measure the orbital properties (orbital period, eccentricity, and masses)

* E-mail: cecilia.sgalletta@sissa.it

† E-mail: giuliano.iorio@unipd.it

‡ E-mail: michela.mapelli@unipd.it

to a high level of accuracy (Kaspi et al. 1994; Stairs et al. 2002; Kramer et al. 2006; Lorimer 2008; Özel et al. 2016; Kramer et al. 2021). Thanks to this property of radio pulsars, we have detected about a dozen of binary NSs (BNSs) in the Milky Way (MW), i.e. binary systems in which both components are NSs (Hulse & Taylor 1975; Burgay et al. 2003; Lyne et al. 2004; Martinez et al. 2015; Özel et al. 2016; Tauris et al. 2017). BNSs are loud sources of GWs (Burgay et al. 2003; Abbott et al. 2017a, 2020; Pol et al. 2019; Radice et al. 2020; Pol et al. 2020; Thrane et al. 2020; Mandel & Broekgaarden 2022; Spera et al. 2022), their merger powers short gamma-ray bursts (Abbott et al. 2017b; Goldstein et al. 2017; Murase et al. 2018; Colombo et al. 2022; Perna et al. 2022) and kilonovae (Tanvir et al. 2013; Smartt et al. 2017; Troja et al. 2017; Kasen et al. 2017; Metzger 2017, 2019; Nedora et al. 2023), and is a fundamental source of chemical enrichment by r-process elements (Eichler et al. 1989; Hotokezaka et al. 2018; Côté et al. 2019; Kobayashi et al. 2023; Fujibayashi et al. 2023; Combi & Siegel 2023).

The formation of a BNS from the evolution of a massive binary star is still controversial (e.g., Tauris et al. 2017; Vigna-Gómez et al. 2018; Kruckow et al. 2018; Chruslinska et al. 2018; Giacobbo & Mapelli 2018; Belczynski et al. 2018; Neijssel et al. 2019; Andrews & Mandel 2019; Chattopadhyay et al. 2020; Vigna-Gómez et al. 2020; Belczynski et al. 2020; Olejak et al. 2021; Riley et al. 2022; Broekgaarden et al. 2022; Olejak et al. 2022; Iorio et al. 2022). According to the standard scenario, the two progenitor stars undergo at least one Roche-lobe overflow, after which the first SN takes place, leading to the formation of the first NS. If the binary system is tight enough to avoid disruption by the natal kick, the evolution of the companion star then initiates a common envelope (CE) phase, which results in the ejection of the envelope and the formation of a tight binary system composed of a NS and a naked He star. If such system avoids disruption even during the second SN, a BNS forms, which might then harden by GW emission until it reaches coalescence (Tauris et al. 2017, and references therein). An alternative scenario consists in an early CE phase between the two progenitor stars, leading to the formation of a binary system composed of two naked cores onto a very tight orbit. Such binary system might avoid ionization during the two SN explosions and lead to the formation of a BNS (Brown 1995; Dewi et al. 2006; Justham et al. 2011; Vigna-Gómez et al. 2018, 2020; Broekgaarden et al. 2021; Iorio et al. 2022).

Two of the most important unknowns of binary star evolution are the physics of CE (Ivanova et al. 2013; Klencki et al. 2021; Roepke & De Marco 2022) and the natal kick (Woosley 1987; Janka & Mueller 1994; Lai et al. 2001; Hobbs et al. 2005; O’Doherty et al. 2023). CE (Paczynski 1976; Webbink 1985) is usually described with a simple energy formalism, in which we assume that a fraction α of the kinetic orbital energy of the two cores is transferred to the envelope and helps unbinding it (see e.g. Nelemans et al. 2000; Hirai & Mandel 2022; Di Stefano et al. 2023, for alternative models). The distribution of natal kicks is often modelled with a Maxwellian curve with one-dimensional root-mean square $\sigma = 265 \text{ km s}^{-1}$, based on the proper motions of 73 young Galactic radio pulsars (Hobbs et al. 2005). However, core-collapse SN models suggest that the kick might be much lower in presence of a stripped or ultra-stripped SN, i.e. a SN triggered by a naked He or CO core (Tauris et al. 2015, 2017; Bray & Eldridge 2016, 2018; Giacobbo & Mapelli 2020). Moreover, electron-capture SNe, especially in binary systems, might be associated with low kicks (Gessner & Janka 2018; Giacobbo & Mapelli 2019; Müller et al. 2019; Stevenson et al. 2022).

The aim of this work is to characterize the population of Galactic BNSs, by using a population synthesis code coupled with a MW model. We evolve the orbital binary properties, the spin period and

magnetic field of pulsars. With this framework, we explore the merger rates, the orbital properties and the population of radio pulsars. We consider many different assumptions for the MW model, the magnetic field, and the binary population parameters. We compare our models with current observations of Galactic BNSs.

To this purpose, we use the state-of-the-art population synthesis code `SEVN` (Spera & Mapelli 2017; Spera et al. 2019; Mapelli et al. 2020; Iorio et al. 2022) to implement single and binary stellar evolution. We adopt four MW models, employing semi-empirical prescriptions (Chiappini et al. 1997; Courteau et al. 2014; Pezzulli & Fraternali 2015; Grisoni et al. 2017; Boco et al. 2019) and cosmological simulations (Schaye et al. 2014; The EAGLE team 2017; Nelson et al. 2019a,b). We explore several parameters, such as α , the birth distribution of spin periods and surface magnetic fields of pulsars, and the magnetic field decay timescale. We test our results against the observed Galactic pulsar population.

2 METHODS

We study the Galactic BNS population by coupling various MW models with BNS catalogues obtained with the `SEVN` population synthesis code. Here below, we present the details of our models.

2.1 SEVN

The stellar evolution for N-body (`SEVN`) code is a state-of-the-art binary population synthesis code that implements single stellar evolution by interpolating pre-computed stellar tracks on the fly, and binary processes through analytic and semi-analytic models (Spera & Mapelli 2017; Spera et al. 2019; Mapelli et al. 2020). We use the latest version of the `SEVN` code, described in Iorio et al. (2022)¹. In the following, we will give a general overview of the main features of `SEVN` focusing on the processes most relevant for this work. We refer to Iorio et al. (2022) for a detailed description of the code. The first distinctive mark of `SEVN` is the way it handles single stellar evolution: the interpolation of look-up tables makes `SEVN` fast and versatile. In fact, it is possible to change stellar evolution models by simply substituting the input stellar track tables. The stellar tracks adopted in this work have been evolved with the `PARSEC` code² (Bressan et al. 2012; Costa et al. 2019; Costa et al. 2021; Nguyen et al. 2022).

`SEVN` includes several prescriptions for core-collapse SN explosions. In this work, we investigate the impact on our results of three of them: the *rapid* and *delayed* models by Fryer et al. (2012) and the *rapid-Gauss* model. The rapid and the delayed models are both based on a convection-enhanced neutrino-driven mechanism for the SN explosion, though the revival of the shock wave happens within the first 250ms after the collapse in the rapid model, whereas such timescale can be much longer for the delayed model. The two prescriptions predict the masses of compact remnants as the sum of the mass of the proto-compact object and the amount of fallback material. The third model we adopted is based on the rapid explosion mechanism but draws the NS masses from a Gaussian distribution peaked at $1.33 M_{\odot}$ with standard deviation $0.09 M_{\odot}$, resulting from a fit to the Galactic BNS masses (Özel et al. 2012, 2016). We decided to introduce this model because both the rapid and delayed prescriptions

¹ `SEVN` is publicly available at <https://gitlab.com/sevncodes/sevn.git>. The version used in this work is the release *Sgalletta23*: <https://gitlab.com/sevncodes/sevn/-/releases/sgalletta23>.

² We adopt the tables labelled *SEVNtracks_parsec_ov05_AGB* for the H-stars and *SEVNtracks_parsec_pureHe36* for the naked He stars.

fail to reproduce the observed NS mass distribution (Vigna-Gómez et al. 2018). In the delayed, rapid, and rapid-Gauss models, we do not allow for NS masses $< 1.1 M_{\odot}$. `sevn` assumes that if a compact remnant has mass $\in [1.1, 3) M_{\odot}$ it is a NS, whereas if it has a mass $\geq 3 M_{\odot}$ it is a black hole. The NS radius is fixed at 11 km (Özel et al. 2012; Bogdanov et al. 2016; Bauswein et al. 2017; Abbott et al. 2018).

`sevn` includes several formalisms to model natal kicks. Here, we draw black hole natal kicks following Giacobbo & Mapelli (2020):

$$V_{\text{kick}} = f_{\text{H05}} \frac{\langle M_{\text{NS}} \rangle}{M_{\text{rem}}} \frac{M_{\text{ej}}}{\langle M_{\text{ej}} \rangle}, \quad (1)$$

where $\langle M_{\text{NS}} \rangle$ and $\langle M_{\text{ej}} \rangle$ are the average NS mass and ejecta mass from single stellar evolution, respectively, while M_{rem} and M_{ej} are the compact object mass and the ejecta mass (Giacobbo & Mapelli 2020). The term f_{H05} is a random number drawn from a Maxwellian distribution with one-dimensional root mean square $\sigma_{\text{kick}} = 265 \text{ km s}^{-1}$, coming from a fit to the proper motions of 73 young pulsars (< 3 Myr) in the MW (Hobbs et al. 2005). In this formalism, stripped and ultra-stripped SNe result in lower kicks with respect to the other explosions, owing to the lower amount of ejected mass M_{ej} (Bray & Eldridge 2016, 2018). In addition to the natal kick, we also calculate a Blaauw kick (Blaauw 1961) resulting from the instantaneous mass loss in a binary system triggered by a SN explosion. We use the same formalism as described in Appendix A of Hurley et al. (2002).

2.2 Binary evolution

In the following, we focus on the binary evolution processes implemented in `sevn` that are relevant for this work, especially Roche-lobe overflow (RLO) and the CE phase (Iorio et al. 2022). The Roche lobe of a star in a binary system defines the region of space within which matter is gravitationally bound to the star itself. Therefore, when a star fills its Roche lobe, matter flows to the companion object under its gravitational attraction. This process is known as RLO. RLO thus involves variations in the mass ratio, in the masses and radii of the two stars and in the semi-major axis of the system. At each timestep, `sevn` evaluates the Roche-lobe radius of the two stars in the binary system using the analytical expression derived in Eggleton (1983):

$$\frac{R_L}{a} = \frac{0.49 q^{2/3}}{0.6q^{2/3} + \ln(1 + q^{1/3})}, \quad (2)$$

where q is the mass ratio and a is the semi-major axis. If either star radii satisfy the condition $r \geq R_L$, a RLO episode initiates and mass falls from the donor (the star filling its Roche lobe) to the accretor. Depending on the response of the Roche-lobe and donor radius to mass stripping, mass transfer can be stable or unstable. To assess the stability of mass transfer, `sevn` adopts a formalism common to many population synthesis codes (see e.g. Hurley et al. 2002; Hobbs et al. 2005). The mass ratio of the donor d star to the accretor a star, q , is compared to a critical value q_c , dependent on the stellar evolutionary phase of the donor star: if $q > q_c$ the mass transfer is unstable on a dynamical timescale. Here, we use the values of q_c adopted in the fiducial simulations of (Iorio et al. 2022, see their Table 3). In this model, mass transfer is always stable if the donor star is in the main sequence or in the Hertzsprung gap evolutionary phase. In the case of stable mass transfer, the mass loss rate in `sevn` scales as (Hurley et al. 2002)

$$\dot{M}_d = -F(M_d) \left(\ln \frac{R_d}{R_{L,d}} \right)^3 M_{\odot} \text{ yr}^{-1}, \quad (3)$$

where $F(M_d)$ is a normalization factor, R_d is the radius of the donor and $R_{L,d}$ is the Roche lobe of the donor star. `sevn` allows for non conservative mass transfer; therefore, the mass lost by the donor can be bigger than the amount accreted by the companion. The mass accreted is modeled as follows:

$$\dot{M}_a = \begin{cases} \min(\dot{M}_{\text{Edd}}, -f_{\text{MT}} \dot{M}_d) & \text{if the accretor is a compact object} \\ -f_{\text{MT}} \dot{M}_d & \text{otherwise,} \end{cases} \quad (4)$$

where \dot{M}_{Edd} is the Eddington rate and $f_{\text{MT}} \in [0, 1]$ is the mass accretion efficiency. We set $f_{\text{MT}} = 0.5$ in our simulations (Bouffanais et al. 2021; Iorio et al. 2022).

When mass transfer is unstable the outcome can be either a stellar merger or a CE. During the CE phase, the cores of the two stars orbit each other within a shared envelope. `sevn` parametrizes the CE phase using the α formalism (Webbink 1985; Tout et al. 1997). The envelope's binding energy at the onset of the CE is evaluated as:

$$E_{\text{bind},i} = -G \left(\frac{M_1 M_{\text{env},1}}{\lambda_1 R_1} + \frac{M_2 M_{\text{env},2}}{\lambda_2 R_2} \right), \quad (5)$$

where M is the mass of the star, M_{env} is the mass of the envelope, and R is the star's radius. The subscripts 1 and 2 refer to the primary and secondary star, respectively. Finally, λ takes into account the structural properties of the envelope of each star, which is calculated following the model by Claeys et al. (2014), as described in Appendix A of Iorio et al. (2022). The variation of the orbital energy is

$$\Delta E_{\text{orb}} = \frac{G M_{c,1} M_{c,2}}{2} \left(a_f^{-1} - a_i^{-1} \right), \quad (6)$$

where $M_{c,1}$ and $M_{c,2}$ are the core masses of the two stars and a_i and a_f are the semi-major axis at the onset and at the end of the CE, respectively. `sevn` infers the values of a_f through the condition $E_{\text{bind},i} = \alpha \Delta E_{\text{orb}}$. The α parameter represents the efficiency of energy transport from the binary orbit to the envelope. According to its original definition, α should take values between 0 and 1, but recently values of $\alpha > 1$ have been explored, to account for the missing physics in this very simplified formalism (e.g., Fragos et al. 2019). If the core radii of the two stars are both smaller than their Roche lobes at the end of CE (Eq. 2), then the envelope is ejected. Otherwise, the two stars merge during the CE phase.

2.3 NS properties

To study the evolution of the physical properties of NSs with `sevn`, at the time of formation we assign to each NS a spin, a magnetic field and an angle between the rotation and the magnetic axis, α_B . For all of our NSs, we generate $\cos \alpha_B$ from an uniform distribution between 0 and 1. The evolution of each NS depends on its interaction with the companion star. If the NS is not accreting matter from the companion, the evolution is the same as if the NS were isolated, i.e. the NS spin and magnetic field decrease with time (*spin down*). In contrast, if the companion star fills its Roche lobe, the infalling matter can transfer angular momentum to the NS, causing the latter to spin up. When the latter process takes place the resulting NS is said to be *recycled*. In fact, observed recycled pulsars are usually characterized by short spin periods and relatively low magnetic fields (Lorimer 2008; Lorimer 2011; Özel et al. 2016).

2.3.1 Spin down

If the evolution of the pulsar proceeds unperturbed, the pulsar can be seen as a rotating magnet. We model the magnetic field of the pulsar

with a dipole and compute the loss of energy accordingly. In fact, as the pulsar rotates it emits electromagnetic radiation, losing rotational energy, that is the pulsar spins down. The angular frequency of the pulsar changes according to [Goldreich & Julian \(1969\)](#):

$$\dot{\Omega} = -\frac{8\pi B^2 R^6 \sin^2 \alpha_B \Omega^3}{3\mu_0 c^3 I}, \quad (7)$$

where Ω is the angular frequency, B is the surface magnetic field, R is the radius, α_B is the angle between the rotational axis and the magnetic axis, I is the moment of inertia of the pulsar, c is the speed of light, and μ_0 is the vacuum magnetic permeability. The time derivative of the angular frequency $\dot{\Omega}$ is linked to Ω through the relation $\dot{\Omega} \propto \Omega^n$, where n is the magnetic braking index. Observational evidence points toward a value of n lying in the range 2.5 – 3.5 ([Manchester et al. 2005](#)). In addition, we assume that the magnetic field decays with time because of Ohmic dissipation. The finite resistivity in the NS crust, caused by electron scatterings, converts the magnetic energy into heat ([Goldreich & Reisenegger 1992](#); [Konar & Bhattacharya 1997](#); [Urpin & Kononkov 1997](#); [Konar & Bhattacharya 1999](#)). Furthermore, observations seem to support the decay of the magnetic field: younger pulsars show in general stronger magnetic fields with respect to older ones ([Ostriker & Gunn 1969](#)). In our models, we evolve the magnetic field following an exponential decay ([Kiel et al. 2008](#); [Osłowski et al. 2011](#); [Chattopadhyay et al. 2020, 2021](#)):

$$B = (B_0 - B_{\min}) e^{-t/\tau_d} + B_{\min}, \quad (8)$$

where B_0 is the initial surface magnetic field, B_{\min} is the minimum surface magnetic field strength and τ_d is the magnetic field decay timescale. We assume that the pulsar magnetic field stops decreasing when it reaches the value B_{\min} . Throughout this work, we adopt $B_{\min} = 10^8$ G, as suggested by [Zhang & Kojima \(2006\)](#). The magnetic field decay timescale τ_d is a free parameter of the model. Its value is controversial: ranging from 2 – 5 Myr (e.g., [Osłowski et al. 2011](#)) to 2000 Myr (e.g., [Kiel et al. 2008](#)). [Faucher-Giguère & Kaspi \(2006\)](#) carry out their analysis considering no magnetic field decay at all.

Following [Chattopadhyay et al. \(2020\)](#), we get an analytic expression for the evolution of the angular frequency of the pulsar:

$$\frac{1}{\Omega_f^2} = \frac{1}{\Omega_i^2} + \frac{16\pi R^6 P \sin^2 \alpha_B}{3\mu_0 c^3 I} \times \left[B_{\min}^2 \Delta t - \tau_d B_{\min} (B_f - B_i) - \frac{\tau_d}{2} (B_f^2 - B_i^2) \right], \quad (9)$$

where Ω_i and Ω_f are the initial and final angular frequencies, B_i and B_f are the initial and final magnetic fields, and Δt is the time elapsed between the final and the initial states.

The spin period P and the spin down rate \dot{P} can then be obtained from Ω and $\dot{\Omega}$ through the following relations:

$$P = \frac{2\pi}{\Omega} \quad (10)$$

$$\dot{P} = -\frac{\dot{\Omega} P}{\Omega}. \quad (11)$$

We update the values of the NS spin periods and magnetic fields in `SEVN` after each time-step according to Eqs. 8 and 9. We can trace the pulsar evolution in the $P - \dot{P}$ diagram. Because of spin down, pulsars evolve towards larger spin periods and lower magnetic fields. In the $P - \dot{P}$ plane, this trend results in a diagonal shift, towards the lower right corner of the plot (see e.g. Figure 2 in [Chattopadhyay et al. 2020](#)). The timescale of this evolution depends on the choice of τ_d : for shorter values of τ_d the traversal of the $P - \dot{P}$ plane is faster.

2.3.2 Spin up

Matter exchange processes in binary stars, such as those happening during a RLO, can significantly affect the evolution of NS spin and magnetic field. For instance, part of the angular momentum of the exchanged material, can be transferred to the NS, that, consequently, spins up. In `SEVN`, we have implemented the spin-up process of NSs during RLO mass transfer following the same prescriptions as in [Kiel et al. \(2008\)](#) and [Chattopadhyay et al. \(2020\)](#). The rate of change in the angular momentum of the pulsar \dot{J}_{acc} scales linearly with the amount of accreted mass, that is:

$$\dot{J}_{\text{acc}} = \epsilon V_{\text{diff}} R_A^2 \dot{M}_{\text{NS}}, \quad (12)$$

where ϵ is an efficiency factor, set at 1 in our models, \dot{M}_{NS} is the mass accretion rate on the NS, and R_A is the magnetic radius. We define $R_A = R_{\text{Alfven}}/2$ as in [Chattopadhyay et al. \(2020\)](#). The Alfvén radius R_{Alfven} is the radius at which the magnetic pressure equals the ram pressure:

$$R_{\text{Alfven}} = \left(\frac{2\pi^2}{G\mu_0^2} \right)^{1/7} \times \left(\frac{R^6}{\dot{M}_{\text{NS}} M_{\text{NS}}^{1/2}} \right)^{1/7} \times B^{4/7}. \quad (13)$$

V_{diff} is the difference between the Keplerian angular velocity at the magnetic radius $\Omega_{\text{K}}|_{R_A}$ and the co-rotation angular velocity Ω_{co} :

$$V_{\text{diff}} = \Omega_{\text{K}}|_{R_A} - \Omega_{\text{co}}. \quad (14)$$

We can see from Eq. 12, that the condition for the NS to spin up is $V_{\text{diff}} > 0$. In this case, the variation in angular momentum of the NS is positive and its spin increases: as matter reaches the magnetic radius, the magnetic pressure dominates and matter follows the magnetic field lines and is accreted on the NS polar caps. In contrast, if $V_{\text{diff}} < 0$, then the NS acts as a propeller ([Kiel et al. 2008](#)): the velocity of the magnetic field lines at the magnetic radius is higher than the local Keplerian velocity ($\Omega_{\text{co}} > \Omega_{\text{K}}|_{R_A}$) and matter is blown away from the NS ([Illarionov & Sunyaev 1975](#)). In `SEVN`, we have implemented the propeller effect as well.

We also assume that the magnetic field decays exponentially with the amount of mass accreted. Observations of the low magnetic fields of binary and millisecond pulsars suggest accretion-induced field decay ([Konar & Bhattacharya 1997](#)). The magnetic field evolves according to the following equation during RLO in our models:

$$B = (B_0 - B_{\min}) \times \exp\left(-\frac{\Delta M_{\text{NS}}}{\Delta M_d}\right) + B_{\min}. \quad (15)$$

ΔM_{NS} is the amount of mass accreted by the NS and ΔM_d is the magnetic field decay mass scale, another free-parameter of the model. We fixed ΔM_d to the fiducial value $\Delta M_d = 0.025 M_{\odot}$, which corresponds to the optimal value obtained in [Chattopadhyay et al. \(2020\)](#). We further discuss the values adopted in our simulations in Sec. 2.7.

At each time-step, `SEVN` evaluates if matter accretes onto the NS via RLO. If not, the variations to the spin and magnetic field of the NS are only due to spin down (Eqs. 7 and 8). Otherwise, the algorithm first evaluates V_{diff} . If $V_{\text{diff}} > 0$, `SEVN` calculates also the spin up from Eqs. 12 and 15:

$$\Omega_{i+1} = \Omega_i + \frac{\Delta J_{\text{acc}}}{I}, \quad (16)$$

where $\Delta J_{\text{acc}} = V_{\text{diff}} R_A^2 \Delta M_{\text{NS}}$. At the end of the time-step, `SEVN` updates both the spin and the magnetic field accordingly. If $V_{\text{diff}} < 0$, no matter accretes during that time-step and spin and magnetic fields are updated only accounting for spin down. This accurate treatment

of spin up and down benefits from the adaptive time-step formalism of SEVN (Iorio et al. 2022).

According to Chattopadhyay et al. (2020), a CE phase can trigger further spin up of the NS, as suggested by MacLeod & Ramirez-Ruiz (2015). Here, we decide not to include this possible spin up by CE, because it is quite controversial (Osłowski et al. 2011; Chamandy et al. 2018).

2.4 Initial conditions for the SEVN binary catalogues

We sample the masses of the primary stars (M_1) from a Kroupa’s initial mass function (Kroupa 2001), in a range between 5 and $150M_\odot$:

$$\mathcal{F}(M) \propto M_1^{-2.3} \quad (17)$$

We draw the secondary star’s mass (M_2), the initial binary orbital period (P_{orb}), and the eccentricity following the distributions derived by Sana et al. (2012), which are based on observations of massive binary stars in young clusters:

$$\mathcal{F}(q) \propto q^{-0.1} \quad (18)$$

where $q = M_2/M_1 \in [q_{\text{min}}, 1]$, $q_{\text{min}} = \max\left(\frac{2.2M_\odot}{M_1}, 0.1\right)$, so that the secondary star mass distribution is cut at $2.2M_\odot$,

$$\mathcal{F}(P_{\text{orb}}) \propto (\log P_{\text{orb}})^{-0.55} \quad (19)$$

with $0.15 \leq \log(P_{\text{orb}}/d) \leq 5.5$, and

$$\mathcal{F}(e) \propto e^{-0.42} \quad (20)$$

with $0 \leq e \leq 0.9$. For each parameter (described in section 2.7), we simulate with SEVN 11 sub-sets varying the metallicity: $Z = 0.0002, 0.0004, 0.0008, 0.0012, 0.0016, 0.002, 0.004, 0.008, 0.012, 0.016, 0.02$. Each SEVN sub-set evolves 10^6 binary systems. Therefore, for each model we ran a total of 1.1×10^7 binaries.

2.5 Milky Way (MW) models

In our work, we couple the catalogues of binary NS systems from SEVN with a MW-like galaxy. We choose four Galaxy models that have total stellar mass and current star formation rate (SFR) as close as possible to the measured values of the MW (Artale et al. 2019). Therefore, we require a total stellar mass $(5.43 \pm 0.57) \times 10^{10} M_\odot$ (McMillan 2017) and a current SFR $\sim 1.65 M_\odot \text{ yr}^{-1}$ (Licquia & Newman 2015). The use of different Galaxy models allows us to test the robustness of our results against the specific features of the chosen MW models. Here below, we describe the four models in detail. We summarize them in Table 1.

2.5.1 Constant SFR (Const model)

The first model for the MW assumes a constant SFR, fixed at $1.65 M_\odot \text{ yr}^{-1}$. All binary systems in this model have solar metallicity, $Z = 0.0142$ (Asplund et al. 2009; Vigna-Gómez et al. 2018; Chattopadhyay et al. 2020). The integration of the SFR through cosmic time leads to a total stellar mass $M_\star \sim 1.9 \times 10^{10} M_\odot$, well below the observed value. This MW model has been used by most of the previous works (e.g., Vigna-Gómez et al. 2018; Shao & Li 2018; Chattopadhyay et al. 2020), adopting a fixed SFR at $1 M_\odot \text{ yr}^{-1}$.

2.5.2 The EAGLE model

The EAGLE project³ (Schaye et al. 2014; The EAGLE team 2017) comprises a set of cosmological hydrodynamical simulations with comoving box sizes of 25, 50 and 100 Mpc, evolved from redshift $z = 20$ to $z \sim 0$. The simulations are run with the GADGET-3 code (Springel 2005). A full description of the sub-grid baryonic processes included can be found in Schaye et al. (2014). The cosmological framework adopted is the Λ CDM cosmological model, with cosmological parameters: $\Omega_{\Lambda,0} = 0.693$, $\Omega_{M,0} = 0.307$, $\Omega_{b,0} = 0.048$, $\sigma_8 = 0.8288$, $n_s = 0.9611$, and $h = 0.6777$ (Ade et al. 2014). We selected a MW-like galaxy from the EAGLE run labeled L025N0752, characterized by a periodic box of side 25 Mpc comoving. This is the run with the highest resolution in the EAGLE suite: the baryonic particle and the dark matter mass resolutions are $2.26 \times 10^5 M_\odot$ and $1.21 \times 10^6 M_\odot$, respectively. By imposing the requirements outlined in Section 2.5, we selected a best-fitting galaxy identified by the IDs of the halo, Gnr = 23 and the sub-halo, Sgrn = 0. This galaxy is characterized by a total stellar mass $3.65 \times 10^{10} M_\odot$ and a current SFR $1.38 M_\odot \text{ yr}^{-1}$.

2.5.3 The ILLUSTRISTNG model

The ILLUSTRISTNG project⁴ consists of three simulation volumes, with comoving box size of 50, 100 and 300 Mpc, from redshift $z = 127$ to $z \sim 0$. The simulations have been run with the moving mesh code AREPO (Springel 2010). A full description of the baryonic processes included in this simulation can be found in Nelson et al. (2019a) and Pillepich et al. (2019). A Λ CDM cosmological model is assumed, with cosmological parameters from Ade et al. (2016): $\Omega_{\Lambda,0} = 0.6911$, $\Omega_{M,0} = 0.3089$, $\Omega_{b,0} = 0.0486$, $\sigma_8 = 0.8159$, $n_s = 0.9667$ and $h = 0.6774$. We select our MW-like galaxy from the TNG50 run (with 50 Mpc comoving length, Nelson et al. 2019b). The best candidate galaxy for our work is identified by Gnr = 244 and Sgrn = 547844, with a total stellar mass $5.10 \times 10^{10} M_\odot$ and current SFR $1.675 M_\odot \text{ yr}^{-1}$. The galaxy is included in the MW-type catalog released by Pillepich et al. (2023) from the TNG50 simulation.

2.5.4 The empirical (Emp) model

We also include a MW-like model built from empirical relations. We adopt an exponentially decaying SFR function:

$$\text{SFR}(\tau) = A \exp(-\tau/\tau_\psi) \quad (21)$$

where A is a proportionality constant, τ is the internal Galactic age, defined as the time t_f elapsed since the beginning of significant star formation activity in the Galaxy, and τ_ψ is the characteristic timescale for the suppression of SFR (Grisoni et al. 2017; Bovy 2017; Boco et al. 2019). This model is commonly adopted to describe low-redshift, disc-dominated galaxies (Chiappini et al. 1997; Courteau et al. 2014; Pezzulli & Fraternali 2015; Grisoni et al. 2017). Integrating the SFR over the cosmic time yields the total stellar mass of the galaxy:

$$M_\star(t_0) = \int_{t_f}^{t_0} \text{SFR}(t) dt, \quad (22)$$

where t_0 is the cosmic time today. For our MW-like galaxy, we set $\tau_\psi = 7 \text{ Gyr}$, as the SFR decay timescale (Bovy 2017). To derive the

³ <https://icc.dur.ac.uk/Eagle/>

⁴ <https://www.tng-project.org/>

two unknowns in Equations 21 and 22, A and t_f , we imposed a total stellar mass $M_\star(t_0) = 5 \times 10^{10} M_\odot$ and a current star formation rate $\text{SFR}(t_0) = 1.65 M_\odot \text{ yr}^{-1}$.

As for the metallicity evolution, we assume the fundamental metallicity relation (FMR, Mannucci et al. 2010, 2011). The FMR has been obtained empirically through observations of the local galaxies of the Sloan Digital Sky Survey, and its robustness has been confirmed for galaxies up to $z \sim 3.5$ (Mannucci et al. 2010; Hunt et al. 2016). The FMR links M_\star , SFR and the gas metallicity Z , whereas it is almost independent of redshift (Chruslińska et al. 2021; Boco et al. 2021; Santoliquido et al. 2022). Following this approach, the Galaxy metallicity is evaluated through Eq. 2 of Mannucci et al. (2011):

$$12 + \log(\text{O}/\text{H}) = \begin{cases} 8.90 + 0.37 m - 0.14 s - 0.19 m^2 & \text{for } \mu_{0.32} \geq 9.5 \\ \quad + 0.12 m s - 0.054 s^2 & \\ 8.93 + 0.51 (\mu_{0.32} - 10) & \text{for } \mu_{0.32} < 9.5 \end{cases} \quad (23)$$

with $\mu_{0.32} = \log M_\star - 0.32 \log \text{SFR}$, $m = \log M_\star - 10$, and $s = \log \text{SFR}$. We build our empirical model by evaluating the SFR (Eq. 21) and the metallicity at a series of time-steps, ranging from ~ 12 Gyr ago until today. At each time-step, we assume that the metallicity follows a log-normal distribution within the Galaxy, with mean equal to the value predicted by the FMR (Eq. 23) and variance $\sigma_{\log Z} = 0.1$ dex.

2.6 Populating the MW with BNSs

To populate the MW galaxy models with the catalogues of BNSs evolved with SEVN, we follow the same procedure as outlined in Mapelli et al. (2017) and Mapelli & Giacobbo (2018). For each simulation set, we read the eccentricity e and the semi-major axis a of the binary, the times of the SN explosions t_1 and t_2 , the NS masses m_1 and m_2 , the spin periods P_1 and P_2 and magnetic fields B_1 and B_2 at the formation of the second compact object. Along with this, we save the total simulated initial stellar mass M_{SEVN} for each of the 11 metallicity sub-sets.

For the EAGLE and ILLUSTRISTNG models, we read every stellar particle from the snapshot of the Galaxy at redshift $z = 0$. In particular, we need the stellar particle mass m_\star , its formation redshift z_\star , and its metallicity at formation Z_\star . For each stellar particle, we select the SEVN catalogue with the metallicity closest to Z_\star , and associate to it a number of BNSs proportional to the ratio m_\star/M_{SEVN} :

$$n_{\text{BNS}} = N_{\text{SEVN}} \frac{m_\star}{M_{\text{SEVN}}} f_{\text{corr}} f_{\text{bin}}, \quad (24)$$

where N_{SEVN} is the number of BNSs within the selected catalogue, f_{corr} , and f_{bin} are correction factors. The factor $f_{\text{corr}} = 0.285$ takes into account that we consider only systems with primary star mass $\geq 5 M_\odot$. By integrating the Kroupa IMF between 0 and $5 M_\odot$, we obtain the relative weight of stars with a mass $\geq 5 M_\odot$: this yields $f_{\text{corr}} = 0.285$. The factor f_{bin} corrects for the binary fraction, i.e. takes into account that we evolve only binary systems. From Sana et al. (2012), $f_{\text{bin}} = 0.4$, which is equivalent to saying that 40% of stellar mass lie in binary systems. We randomly choose, with a Monte Carlo-like approach, n_{BNS} BNSs from the SEVN catalogue.

For the empirical model, we do not have stellar particles, but we can derive the amount of stellar mass formed by the Galaxy ΔM_\star at each time-step. Knowing the metallicity distribution at the same time-step, we can derive how much mass has been accreted $\Delta m_\star|Z$, for each of the SEVN metallicities. The sum over all the 11 metallicities

is:

$$\Delta m_\star = \sum_{i=1}^{11} \Delta m_\star|Z_i \quad (25)$$

So, for each metallicity we evaluate n_{BNS} simply by substituting the value of $\Delta M_\star|Z_i$ in Eq. 24.

We convert the formation redshift z_\star of each stellar particle in lookback time:

$$t_{\text{lb}}(z) = \frac{1}{H_0} \int_0^z \frac{dz'}{(1+z') \sqrt{\Omega_{\text{M},0} (z'+1)^3 + \Omega_{\Lambda,0}}} \quad (26)$$

choosing the cosmological parameters consistently with the adopted cosmological simulation (Section 2.5). Then, the formation time of a BNS within the Galaxy is⁵

$$t_{\text{BNS}} = t_\star - \max(t_1, t_2), \quad (27)$$

where t_\star is the lookback time of the formation of the stellar particle corresponding to the redshift z_\star . From now on, all the times will be expressed in lookback times.

We assume that the subsequent evolution is driven only by the emission of gravitational wave radiation. Integrating the differential equations for gravitational wave radiation, derived in Peters (1964), we evolve the eccentricity and the semi-major axis:

$$\begin{aligned} \frac{da}{dt} &= -\frac{64 G^3 m_1 m_2 (m_1 + m_2)}{5 c^5 a^3 (1 - e^2)^{7/2}} \left(1 + \frac{73}{24} e^2 + \frac{37}{96} e^4 \right), \\ \frac{de}{dt} &= -\frac{304 G^3 m_1 m_2 (m_1 + m_2)}{15 c^5 a^3 (1 - e^2)^{5/2}} \left(1 + \frac{121}{304} e^2 \right). \end{aligned} \quad (28)$$

For the integration, we employ an Euler method with an adaptive time-step: the time-steps are smaller if the system is rapidly evolving (i.e. close to the merger); if the system is instead on a loose-wide orbit, the integration time-steps are larger. This allows us to have a fast algorithm without losing in precision. We evolve each system from t_{BNS} until today, i.e. $t_{\text{lb}} = 0$. If, during the evolution $a = 3 r_S$, where r_S is the Schwarzschild radius, we assume that the system has merged and do not evolve it anymore.

In parallel, we evolve the NS spin and magnetic field. In particular, we update the spin and magnetic field according to Eqs. 8 and 9, with

$$\Delta t = t_{\text{BNS}} - t_{\text{BNS,final}}, \quad (29)$$

where $t_{\text{BNS,final}} = t_{\text{merge}}$ if the system has merged, or $t_{\text{BNS,final}} = 0$ (i.e., the present time) otherwise. We repeat the same procedure for each parameter set and for each Galaxy model keeping track of both the set of merged BNSs and the population of BNSs today in the MW.

2.7 Simulation set up

We varied several parameters in our model: the SN explosion mechanism prescription (rapid, delayed, rapid-gauss), the CE efficiency parameter α ($\alpha = 0.5, 1, 3, \text{ and } 5$), the initial spin and magnetic-field distributions, and the magnetic field decay timescale τ_d . All the models adopt the rapid-gauss prescription to reproduce the masses of the NSs. In the Appendix A, we test for comparison also the rapid and

⁵ t_1 and t_2 mark the SN explosion times of the primary and secondary progenitor stars, respectively. An episode of mass transfer during the evolution of the system might revert the initial mass ratio, thus leading to $t_1 > t_2$.

MW model	M_{\star} ($10^{10} M_{\odot}$)	SFR ($M_{\odot} \text{ yr}^{-1}$)
EAGLE	3.7	1.38
ILLUSTRISTNG	5.1	1.67
Empirical (Emp)	5.0	1.65
Constant (Const)	1.9	1.65

Table 1. Properties of the MW models. Columns 1 and 2 refer to the total stellar mass M_{\star} and current SFR of the considered Galaxy models.

the delayed models from Fryer et al. (2012). We investigate different values of the parameter α . In particular we set $\alpha = 0.5, 1, 3$, and 5. Both spins and magnetic fields are drawn from initial distributions. We need to make this assumption because the link between the properties of the pre-SN star and those of the NS is highly uncertain. Given the small sample of observed pulsars, the initial distributions are still quite uncertain. There is no agreement in the literature on the favoured initial parameter distributions, see for example Faucher-Giguère & Kaspi (2006); Osłowski et al. (2011). In our work we consider the initial distributions as free parameters and test some of the most common models in the literature, as summarized in Table 2:

(i) *uniform* (hereafter, U): the spin period and the magnetic field are drawn uniformly in the range [10, 100] ms and $[10^{10}, 10^{13}]$ G, respectively.

(ii) *flat-in-log* (hereafter, FL): the spin periods are drawn uniformly between 10 and 100 ms, the magnetic fields are distributed according to a flat-in-log distribution in the range $[10^{10}, 10^{13}]$ G.

(iii) *Faucher-Giguère* (hereafter, FG): spin periods and magnetic fields follow the distributions presented in Faucher-Giguère & Kaspi (2006). The spin periods follow a normal distribution with mean $\langle P \rangle = 300$ ms and variance $\sigma_P = 150$ ms, while the magnetic fields are drawn from a log-normal distribution with mean $\langle \log(B/G) \rangle = 12.65$ and variance $\sigma_{\log B} = 0.55$.

Moreover, we consider different values for the magnetic field decay timescale τ_d (Eq. 8): $\tau_d = 0.1, 0.5, 1$ and 2 Gyr. We test our results on the different MW-like galaxies as well (Section 2.5). We adopt a uniform terminology for our models. Every model is identified with a string built as follows: ‘{distr}a{alpha}t{tau}{MW}’, where within the brackets we substitute the actual value (or acronym) assumed by that specific parameter in the model. So that, in the place of ‘distr’ we substitute the acronym for the initial spins and magnetic fields distributions (see Table 2); ‘alpha’ corresponds to the value α for CE efficiency, ‘tau’ represents the value τ_d of the magnetic field decay timescale, and lastly ‘MW’ the MW-like galaxy chosen. We use the following abbreviations for the MW models: EAGLE, ILLUSTRISTNG, Emp and Const. For example, model ‘Ua3t1Emp’ adopts the uniform distribution of initial spin and magnetic field, $\alpha = 3$, $\tau_d = 1$ Gyr, and the empirical MW model. The models are summarized in Table 3. We choose ‘Ua3t1Emp’ as our fiducial model.

2.8 Selection effects

To compare our modelled BNSs with observations, we need to account for selection effects. For instance, as a pulsar crosses the death line (see section 2.8.1) it ceases to emit in the radio. Furthermore, pulsars have quite narrow beaming opening angles, thus we can only detect the pulsars whose beam intersects the line of sight. Radio selection effects also depend on the sky location of the source. The flux density scales as the inverse of the distance squared, which means that, for a given intrinsic luminosity, observations are biased towards close pulsars. Moreover, scattering by free electrons in the interstellar medium smears the pulsars’ signal, lowering the signal-to-noise

ratio (Cordes & Lazio 2002). Other effects that may affect the observations are pulse nulling and intermittency, i.e. when the pulsed emission ceases for many pulse periods and quasi-periodic on/off cycles, respectively (Lyne et al. 2010). On top of this, the Doppler shifting of the period caused by orbital motion also smears the pulsar signal (Andersen & Ransom 2018; Balakrishnan et al. 2022). We use the python implementation of PSRPOP (Lorimer 2011), PSRPOPpy⁶ (Bates et al. 2014), to account for some of the mentioned selection effects. Specifically, we model the death lines and beam geometry, the dependence on sky location, interstellar radio scintillation, pulsar luminosity and binary selection effects.

2.8.1 Death lines

Pulsars cease to emit in the radio when the magnetic field is not strong enough for the production of electron-positron pairs. The death lines, empirical relations in the $P-\dot{P}$ plane, mark the locus of points beyond which the pulsars stop emitting: if a pulsar crosses one of these lines in the $P-\dot{P}$ plane, it turns off. We adopt the death lines from Rudak & Ritter (1994):

$$\log \dot{P} = 3.29 \log P - 16.55$$

$$\log \dot{P} = 0.92 \log P - 18.65. \quad (30)$$

Moreover, to avoid the piling up of pulsars at the death lines, we also add a cut-off on the efficiency of radio emission as in Szary et al. (2014). The radio efficiency ξ_R is defined as:

$$\xi_R = \frac{L}{\dot{E}}, \quad (31)$$

where L is the pulsar radio luminosity and $\dot{E} = 4\pi^2 I P^{-3} \dot{P}$ is the pulsar spin down power. Following the model by Szary et al. (2014), if the radio efficiency exceeds a certain threshold ($\xi_R > \xi_{R,\max}$), the pulsar ceases to emit. We set the threshold to $\xi_{R,\max} = 0.01$, as in Chattopadhyay et al. (2020, 2021). Following these prescriptions, PSRPOPpy classifies a pulsar as dead if either it has crossed the death lines (Eq. 30) or if $\xi_R > \xi_{R,\max}$.

2.8.2 Beaming fraction

Pulsar radio emission is concentrated on collimated beams with finite width, so that pulsars sweep out only a limited area of the sky. As a consequence, we can detect only a fraction of the whole pulsar population, i.e. those whose beam crosses the observer’s line of sight. The beaming fraction f_{beam} represents the fraction of pulsars beaming towards us. Previous studies agree that f_{beam} is period dependent. We adopt the prescription proposed in Tauris & Manchester (1998), an empirical relation obtained by fitting slow-rotating pulsars ($P \gtrsim 100$ ms),

$$f_{\text{beam}} = 0.09 (\log P - 1)^2 + 0.03 \quad 0 \leq f_{\text{beam}} \leq 1, \quad (32)$$

where P is the spin period of the pulsar in seconds. Equation 32 shows that the beaming fraction is higher for pulsars spinning faster. Therefore such objects are also more likely to be detected. PSRPOPpy takes into account the beaming effects using a rejection sampling method: each pulsar can be detected with a probability f_{beam} , computed according to Eq. 32.

⁶ <https://github.com/samb8s/PSRPOPpy>

Initial Distribution	B_{birth} range (G)	B_{birth} distribution	P_{birth} range (ms)	P_{birth} distribution
U	$(10^{10} - 10^{13})$	Uniform	$(10 - 100)$	Uniform
FL	$(10^{10} - 10^{13})$	Flat in log	$(10 - 100)$	Uniform
FG	–	Faucher-Giguère & Kaspi (2006)	–	Faucher-Giguère & Kaspi (2006)

Table 2. Initial distributions adopted in this work for the spins and magnetic fields.

	α	Init. Distr.	τ_d (Gyr)		α	Init. Distr.	τ_d (Gyr)
Ua0.5t0.1Emp	0.5	U	0.1	Ua3t0.1Emp	3	U	0.1
Ua0.5t0.5Emp	0.5	U	0.5	Ua3t0.5Emp	3	U	0.5
Ua0.5t1Emp	0.5	U	1	Ua3t1Emp	3	U	1
Ua0.5t2Emp	0.5	U	2	Ua3t2Emp	3	U	2
FLa0.5t0.1Emp	0.5	FL	0.1	FLa3t0.1Emp	3	FL	0.1
FLa0.5t0.5Emp	0.5	FL	0.5	FLa3t0.5Emp	3	FL	0.5
FLa0.5t1Emp	0.5	FL	1	FLa3t1Emp	3	FL	1
FLa0.5t2Emp	0.5	FL	2	FLa3t2Emp	3	FL	2
FGa0.5t0.1Emp	0.5	FG	0.1	FGa3t0.1Emp	3	FG	0.1
FGa0.5t0.5Emp	0.5	FG	0.5	FGa3t0.5Emp	3	FG	0.5
FGa0.5t1Emp	0.5	FG	1	FGa3t1Emp	3	FG	1
FGa0.5t2Emp	0.5	FG	2	FGa3t2Emp	3	FG	2
Ua1t0.1Emp	1	U	0.1	Ua5t0.1Emp	5	U	0.1
Ua1t0.5Emp	1	U	0.5	Ua5t0.5Emp	5	U	0.5
Ua1t1Emp	1	U	1	Ua5t1Emp	5	U	1
Ua1t2Emp	1	U	2	Ua5t2Emp	5	U	2
FLa1t0.1Emp	1	FL	0.1	FLa5t0.1Emp	5	FL	0.1
FLa1t0.5Emp	1	FL	0.5	FLa5t0.5Emp	5	FL	0.5
FLa1t1Emp	1	FL	1	FLa5t1Emp	5	FL	1
FLa1t2Emp	1	FL	2	FLa5t2Emp	5	FL	2
FGa1t0.1Emp	1	FG	0.1	FGa5t0.1Emp	5	FG	0.1
FGa1t0.5Emp	1	FG	0.5	FGa5t0.5Emp	5	FG	0.5
FGa1t1Emp	1	FG	1	FGa5t1Emp	5	FG	1
FGa1t2Emp	1	FG	2	FGa5t2Emp	5	FG	2

Table 3. Summary of the simulations. The initial distributions for spins and magnetic fields of NSs (U, FL and FG) are summarized in Table 2. All models listed here have been run within the Empirical MW model. We have explored the same grid of parameters with the other MW models (EAGLE, ILLUSTRISTNG, and Const). All models assume the rapid-Gauss prescription for the SN explosion. Our fiducial model is highlighted in bold text in the Table.

2.8.3 Survey sensitivity

We use the radiometer Equation (Dewey et al. 1985; Lorimer & Kramer 2004) to evaluate the minimum flux that a source must have to be detected

$$S_{\text{min}} = \beta \frac{(S/N_{\text{min}}) (T_{\text{rec}} + T_{\text{sky}})}{G_A \sqrt{n_{\text{pol}}} t_{\text{int}} \Delta\nu} \sqrt{\frac{W}{P - W}}, \quad (33)$$

where S/N_{min} is the minimum signal-to-noise ratio, β takes into account losses in sensitivity due to sampling antenna and digitalisation noise, n_{pol} is the number of polarizations, T_{rec} and T_{sky} are the receiver and sky temperatures, G_A is the antenna gain, $\Delta\nu$ is the observing bandwidth, t_{int} is the integration time, W is the detected pulse width, and P is the pulse period. Most of the latter quantities are survey dependent (e.g. receiver temperature, observing bandwidth, integration time). PSRPOPPLY evaluates the radiometer equation for the Parkes Multibeam Pulsar Survey (Manchester et al. 2001, PM-SURV), the Swinburne Multibeam Pulsar Survey (Edwards et al. 2001, SWINMB), and the High Time Resolution Universe Pulsar Survey (Keith et al. 2010, HTRUP). For each survey, S/N_{min} is fixed to the value set by the survey itself. Moreover, the observed pulsars sample considered in our analyses includes only the objects detected

by the surveys listed above. The effects caused by the propagation of the pulsed signal through the interstellar medium enters Eq. 33 via W . In fact, collisions with free electrons cause a broadening of the received signal. Also, if $W \gtrsim P$ the signal is no longer detectable as the pulse is smeared into the background (Lorimer 2008; Lorimer 2011).

PSRPOPPLY assesses the observed pulse widths from the following relation (Burgay et al. 2003):

$$W^2 = W_i^2 + \tau_{\text{samp}}^2 + \left(\tau_{\text{samp}} \frac{\text{DM}}{\text{DM}_0} \right)^2 + \tau_{\text{scatt}}^2 \quad (34)$$

Here W_i is the intrinsic pulse width, τ_{samp} is the sampling timescale, τ_{scatt} is the mean scattering timescale. DM and DM_0 are the dispersion measures in the direction of the pulsar and the diagonal dispersion of the survey respectively. For simplicity we fix the duty cycle $W_i/P = 0.05\%$ for all pulsars (e.g. Lyne & Manchester 1988).

As the above quantities depend on the sky position of the source, we use the built-in functions of PSRPOPPLY to plant our evolved pulsars in the Galaxy. PSRPOPPLY employs the distribution obtained in Yusifov & Küçük (2004) to assign a radial position to each pulsar. Once assessed the position of the pulsar, the sky noise temperature T_{sky} is evaluated accordingly by fitting the Haslam et al. (1981) Table and rescaling for the correct frequency range (Szary et al. 2014). PSRPOPPLY evaluates

the dispersion measure DM by integrating the electron density n_e over the line of sight. For n_e we adopt the NE2001 model (Cordes 2004). Finally, DM is used to evaluate τ_{scatt} by applying the prescriptions described in Bhat et al. (2004).

The last missing ingredient is the luminosity. We adopt the luminosity function calculated in Faucher-Giguère & Kaspi (2006),

$$\log L = \log L_0 + \alpha_{\text{F06}} \log P + \beta_{\text{F06}} \log(\dot{P}/10^{-15}) + \delta_L, \quad (35)$$

with $L_0 = 0.18 \text{ mJy kpc}^2$, δ_L is drawn from a normal distribution with $\sigma_{\delta_L} = 0.8$, $\alpha_{\text{F06}} = -1.5$ and $\beta_{\text{F06}} = 0.5$.

For each pulsar in the simulated Galactic population, we evaluate both S_{min} and the flux $F = L/(4\pi \mathcal{D}^2)$, where \mathcal{D} is the pulsar distance. A source is detectable if $F > S_{\text{min}}$. We repeat this procedure for each survey, finally combining all the simulated-detected pulsars into a single sample.

2.8.4 Selection effects of binary systems

A comprehensive procedure to account for binary-pulsar selection effects is still unavailable. The Doppler shifting of the period causes a smearing of the signal and thus a reduction in the signal-to-noise ratio (Balakrishnan et al. 2022). This effect is stronger for binary systems with shorter periods and for shorter integration times. The Doppler shifting also depends on the eccentricity of the system. Bagchi et al. (2013) show that the reduction in the signal-to-noise ratio decreases for higher eccentricity. Chattopadhyay et al. (2021) derive a fitting formula from the results of Bagchi et al. (2013). They assume a NS with a mass of $1.4M_{\odot}$, 1000 s duration of observation, and 60° inclination angle; then, fitting via linear regression for eccentricities $e = 0.1, 0.5$ and 0.8 , they find a detection cut-off

$$P_{\text{orb}}/d \geq m \times P/s + c, \quad (36)$$

with

$$m = m_m e + c_m \quad (37)$$

$$c = m_c e + c_c, \quad (38)$$

where $m_m = -8.90$, $c_m = -27.68$, $m_c = -3.40$ and $c_c = 5.72$. Thus, pulsars in shorter orbital period binaries are also the most difficult to be detected. We implement the aforementioned fit (Chattopadhyay et al. 2021) in PSRPOPpy.

2.8.5 Final setup

Using the formalism discussed above we apply the radio selection effects on the final population of BNSs in the MW. We consider only the binaries survived in the MW until the present day and run PSRPOPpy on these catalogues. The code returns the sample of pulsars, picked from the initial catalogue, that are detectable by the selected surveys.

We ran PSRPOPpy multiple times on the total population, in order to filter out stochastic fluctuations. In this way, we obtain multiple realisations of the radio-selected pulsars. This procedure has a further advantage: as a bootstrap technique, it augments the statistic of our final sample.

We repeat this process for each of our models. For each simulation, we compare simulated and observed pulsars, according to three surveys (the Parkes Multibeam Pulsar Survey, Swinburne Multibeam Pulsar Survey, and High Time Resolution Universe Pulsar Survey, Section 2.8). We list the properties of the pulsars considered in this study in Table 4 (Manchester et al. 2005).

2.9 Statistical analysis

We briefly summarize here the main points of the statistical framework used to compare the adopted models. In the following, we will denote the properties of the N_D observed pulsars (orbital period P_{orb} , eccentricity e , spin period P and rate of change of the spin period \dot{P}) with $D = \{P_{\text{orb}}, e, P, \dot{P}\}$, whereas θ_i denotes all the hyper-parameters varied through the models (i.e., the SN explosion mechanism, the CE parameter α , the initial spin and magnetic-field distributions, the magnetic-field decay τ_d , and the MW model) and, by extension, the i -th model itself.

To quantify the relative performance of two competing models in describing the available data, we will compute the Bayes' factor B_{12} ⁷:

$$B_{12} = \frac{P(D, N_D | \theta_1)}{P(D, N_D | \theta_2)}. \quad (39)$$

In general, the likelihood $P(D|\theta)$ requires to evaluate the probability of the available data conditioned on the model. In this case, however, we do not have a functional relationship between the astrophysical hyper-parameters θ and the pulsar's observed parameters.

On the other hand, we have catalogues of simulated observed pulsars, as described in Section 2.8. Each of these catalogues, denoted with $\xi(\theta)$, is composed of N_{ξ} pulsars, representative of the underlying observed distribution on the four pulsar properties. These realisations can be used to reconstruct this distribution and assign a probability for the data D .

The likelihood therefore becomes

$$\begin{aligned} P(D, N_D | \theta) &= \int P(D, N_D | \xi(\theta), N_{\xi}) P(\xi(\theta), N_{\xi} | \theta) d\xi dN_{\xi} = \\ &= \int P(N_D | N_{\xi}) P(D | \xi(\theta)) P(\xi(\theta), N_{\xi} | \theta) d\xi dN_{\xi}. \end{aligned} \quad (40)$$

The first term, $P(N_D | N_{\xi})$, is an inhomogenous Poisson process:

$$P(N_D | N_{\xi}) = \frac{N_{\xi}^{N_D} e^{-N_{\xi}}}{N_D!}. \quad (41)$$

The probability $P(D|\xi(\theta))$ is modelled using a Dirichlet process Gaussian mixture model (DPGMM, e.g., Rinaldi & Del Pozzo 2022a, and references therein). The DPGMM can be used to approximate arbitrary probability densities given a set of samples drawn from the unknown distribution. In particular,

$$P(D|\xi(\theta)) = \int P(D|\lambda) P(\lambda|\xi(\theta)) d\lambda, \quad (42)$$

where λ denotes the parameters of the DPGMM.

Both integrals can be calculated via Monte Carlo approximation, since we are able to sample $\xi(\theta)$ and N_{ξ} using the methods outlined above. Samples for λ , conditioned on a specific realisation of $\xi(\theta)$, are drawn using FIGARO⁸.

With the Monte Carlo approximation, the full likelihood reads

$$\begin{aligned} P(D, N_D | \theta) &\simeq \\ &\frac{1}{M} \sum_{\xi_j(\theta)}^{\xi_M} \left(\frac{(N_{\xi_j}^{N_D} e^{-N_{\xi_j}}) / N_D!}{K} \sum_{\lambda_k | \xi_j(\theta)}^{\lambda_K} \prod_i P(D_i | \lambda_k) \right), \end{aligned} \quad (43)$$

⁷ In general, to do model selection one should compute the odds ratio $O_{12} = B_{12} P(\theta_1) / P(\theta_2)$. However, under the assumption that the two models are a priori equally likely, the odds ratio reduces to the Bayes' factor.

⁸ FIGARO is publicly available at <https://github.com/sterinaldi/figaro>

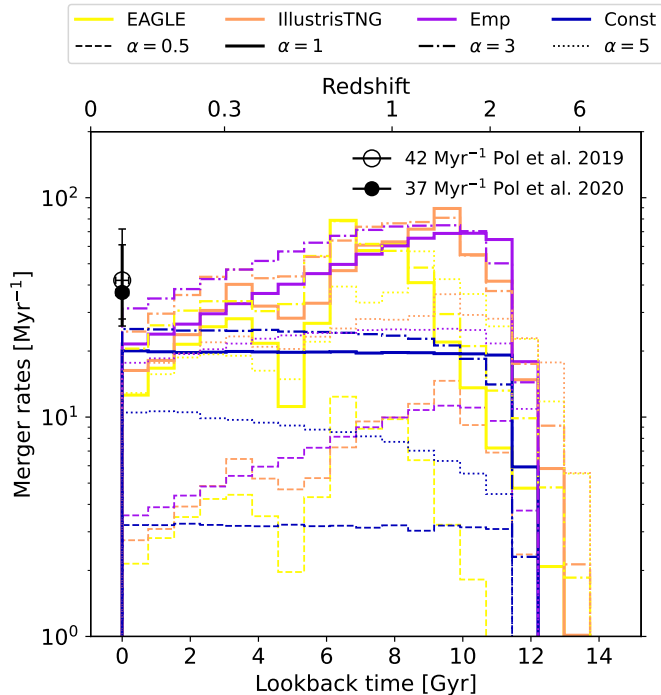


Figure 1. BNS merger rate in the MW as a function of the lookback time for different Galaxy models and values of the CE parameter α . Each colour identifies a Galaxy model. Yellow: EAGLE; pink: ILLUSTRISTNG; purple: Emp; blue: Const. Each line-style is associated with a value of α . Dashed line: $\alpha = 0.5$; solid line: $\alpha = 1$; dash-dotted line: $\alpha = 3$; dotted line: $\alpha = 5$. The circles show the BNS merger rate in the MW inferred from observations: the unfilled circle shows the value by Pol et al. (2019), $\mathcal{R}_{\text{MW}} = 42^{+30}_{-14} \text{ Myr}^{-1}$; the black filled circle shows the updated value by Pol et al. (2020), $\mathcal{R}_{\text{MW}} = 37^{+24}_{-11} \text{ Myr}^{-1}$. All simulations shown in this Figure assume $\tau_{\text{d}} = 1$ Gyr and the U distribution for initial spins and magnetic fields. We do not expect NS spins and magnetic fields to affect the merger rate.

where K denotes the number of draws for λ and M the number of realisations for $\xi(\theta)$, and we made also use of the fact that the observations D are independent.

Using Eq. (43), we can compute the likelihood for each model and, consequently, discriminate between models. If $B_{12} > 1$, the model θ_1 is favoured over model θ_2 . In the following, we will compute the Bayes' factor for each model over our fiducial 'Ua3t1Emp'.

3 RESULTS

3.1 Merger rates

Figure 1 shows the BNS merger rate history for the Galaxy models and for the values of the CE parameter α adopted in this work. Table 5 summarizes the BNS merger rates at present time predicted by our models. For comparison, we also show the BNS merger rate of the MW inferred by Pol et al. (2019, $\mathcal{R}_{\text{MW}} = 42^{+30}_{-14} \text{ Myr}^{-1}$) and Pol et al. (2020, $\mathcal{R}_{\text{MW}} = 37^{+24}_{-11} \text{ Myr}^{-1}$).

The parameter α has a large impact on the BNS merger rate. This result agrees with previous works, showing that almost all BNS mergers form via CE (Tauris et al. 2017; Giacobbo et al. 2018; Kruckow et al. 2018; Vigna-Gómez et al. 2018; Mapelli & Giacobbo 2018; Mapelli et al. 2019; Mandel & Broekgaarden 2022; Iorio et al. 2022). In general, a larger value of α means that energy is transferred more efficiently to the envelope, facilitating its expulsion. In our models,

the highest BNS merger rates are produced for $\alpha = 3$. Different values of α , both higher and lower, yield values of \mathcal{R}_{MW} which are lower than the one inferred from observations by more than one standard deviation.

We find that the merger rate in the local Universe strongly correlates with the SFR of the Galaxy model (Artale et al. 2019). As such, the Galaxy models that better reproduce the observed \mathcal{R}_{MW} are also the ones with the current SFR closer to the one of the MW. In particular, the Emp model with $\alpha = 3$ best reproduces the observed BNS merger rates (see Table 5). For this reason, we choose the Emp model as our fiducial model. In contrast, the EAGLE model underestimates the local BNS merger rate of the MW. In general, the merger rate history follows the same evolution with redshift as the SFR of the host galaxy, since most BNSs merge shortly after their formation. Our findings are in agreement with Artale et al. (2019), who observe a tight correlation between the BNS merger rate and both the mass and the SFR of the host galaxy (see Artale et al. 2019; Artale et al. 2020a,b; Chattopadhyay et al. 2021, for more details on this correlation).

3.2 Orbital period – eccentricity

Figure 2 shows the distributions of our simulated BNSs at lookback time $t_{\text{lb}} = 0$ (today) in the orbital period (P_{orb})–eccentricity (e) plane. We show the results varying α and the host Galaxy model. These plots do not include systems that have merged throughout the history of the MW, but only those that survived until today. All the simulations in Figure 2 have $\tau_{\text{d}} = 1$ Gyr and an uniform (U) distribution for the initial spins and magnetic fields. Indeed, these parameters do not produce significant variations in the final distribution of the $P_{\text{orb}} - e$ plane, as expected. The markers show the observed Galactic pulsars in BNSs systems (Table 4).

Different models in Fig. 2 share similar trends. It is possible to distinguish a main branch characterized by short orbital periods ($\sim 1 - 10^3$ d) and a second one, much less populated, with orbital periods at $\sim 10^{5-6}$ d. At shorter periods, the distributions are bound by the GW merger timescale ($t_{\text{merge}} \lesssim 1$ Myr).

The parameter α has a strong impact on the distribution of BNSs in the $P_{\text{orb}} - e$ plane. In particular, the simulations with $\alpha = 5$ predict about twice as many BNSs as the $\alpha = 3$ model, and roughly five times more binaries compared to the $\alpha = 0.5$ model. This is expected as higher α values are associated with a more efficient expulsion of the CE, therefore more systems are able to survive the CE phase. In contrast, as we decrease α , the probability that a system prematurely merges during the CE increases (Iorio et al. 2022). These plots display another interesting feature: low- α simulations ($\alpha = 0.5, 1$) lack BNSs with low eccentricity, which are instead present in the $\alpha = 3$ and 5 models, favouring more eccentric binaries.

The host Galaxy model also plays a role on the final BNS distribution. In particular, we found that the most important parameter in this case is the total stellar mass M_{\star} of the mock Galaxy. The procedure we adopt to populate a galaxy implies a direct correlation between M_{\star} and the number of BNSs (see Eq. 24). For this reason the Const MW model produces a much lower number of final BNS systems.

Our results qualitatively agree with the observed BNS distribution of orbital periods and eccentricities. A more quantitative comparison is not straightforward owing to observational biases. In fact, eccentric binaries are more difficult to detect (Tauris et al. 2017), having stronger Doppler effects (Chattopadhyay et al. 2021).

Radio pulsar	Type	P (ms)	\dot{P} (10^{-18})	B (10^9 G)	P_{orb} (d)	e	M_{psr} (M_{\odot})	M_{comp} (M_{\odot})	Dist. (kpc)	t_{GW} (Myr)	Survey
J0737-3039 A ^a	recycled	22.7	1.76	2.0	0.102	0.088	1.338	1.249	1.15	86	PMSURV, HTRU
J0737-3039 B ^a	recycled	277.3	892.0	1590	0.102	0.088	1.249	1.338	1.15	86	PMSURV
J1753-2240 ^b	recycled	95.1	0.970	2.7	13.638	0.304	-	-	3.46	$> t_{\text{H}}$	PMSURV, HTRU
J1755-2550 ^c	young	315.2	2430	270	9.696	0.089	-	> 0.40	10.3	$> t_{\text{H}}$	HTRU
J1756-2251 ^d	recycled	28.5	1.02	1.7	0.320	0.181	1.341	1.230	0.73	1660	PMSURV, HTRU
J1757-1854 ^e	recycled	21.5	2.63	7.6	0.184	0.606	1.338	1.395	7.40	78	HTRU
J1811-1736 ^f	recycled	104.2	0.901	3.0	18.779	0.828	< 1.64	> 0.93	5.93	$> t_{\text{H}}$	PMSURV, HTRU
B1913+16 ^g	recycled	59.0	8.63	7.0	0.323	0.617	1.440	1.389	9.80	301	PMSURV

Table 4. Sample of radio pulsars considered in this work. Column 1: pulsar name; column 2: spin P ; column 3: spin derivative \dot{P} ; column 4: magnetic field B ; column 5: orbital period P_{orb} ; column 6: eccentricity e ; column 7: pulsar mass M_{psr} ; column 8: companion mass M_{comp} (here we consider only pulsars which have another NS as companion); column 9: distance from the Sun; column 10: t_{GW} is the merging time of the binary systems, the BNSs with t_{GW} greater than the Hubble time (t_{H}) are shown with $> t_{\text{H}}$. The last column (Column 12) shows in which surveys each pulsar has been discovered, the nomenclature is the same as in Sec. 2.8. References: ^a Kramer et al. (2006); Breton et al. (2008), ^b Keith et al. (2009), ^c Ng et al. (2015, 2018), ^d Faulkner et al. (2004), ^e Cameron et al. (2018), ^f Corongiu et al. (2007), ^g Hulse & Taylor (1975); Weisberg & Huang (2016).

MW model	MERGER RATES (Myr^{-1})			
	α			
	0.5	1	3	5
EAGLE	2.2	12.6	20.5	12.9
ILLUSTRISTNG	2.7	16.3	24.5	16.2
Emp	3.6	21.5	31.3	17.7
Const	3.2	20.0	25.2	10.5

Table 5. BNS merger rate in the MW at present time for different Galaxy models and values of the CE parameter α . All simulations shown in this Figure assume $\tau_{\text{d}} = 1$ Gyr and the U distribution for initial spins and magnetic fields.

3.3 $P - \dot{P}$ plane

Figure 3 shows the distribution of our simulated BNSs at the present time in the $P - \dot{P}$ plane. We show the results varying τ_{d} and the model for the initial spins and magnetic fields. Figure 3 clearly shows the importance of the initial spin and magnetic field distribution on the final pulsar population. Although the number of pulsars in each model varies with α and with the MW model, the shape of the distribution in the $P - \dot{P}$ plane is not significantly affected. Most of the detected BNSs in the MW data are characterized by a spin period ≤ 100 ms. Most of the pulsars in the data-set are probably recycled (Tauris et al. 2017). The primary-born pulsar population in our models do not show striking differences compared to the second-born pulsars.

3.4 Selection effects

Figure 3 shows the intrinsic astrophysical population, without accounting for radio selection effects. In contrast, Figure 4 shows the distribution in the $P - \dot{P}$ plane of the detectable pulsars predicted by our models, obtained as described in Section 2.8 and averaging over $N = 100$ realizations of radio-selected pulsar populations. Figure 4 shows the iso-density contours for models varying τ_{d} and the initial distributions of spins and magnetic fields (U, FL, and FG). The shapes of the contours depend on the chosen initial spins and magnetic fields: the pulsar density peak shifts in the parameter space because of these two parameters. The FG distribution generally produces slower spinning pulsars, with larger values of the spin periods P . In contrast, the FL distribution models peak at $P \sim 0.1$ s, where the majority of the observed pulsars lies. The U distribution, our fiducial model, shows a broader profile spanning a wider range of spin periods with respect to the other models.

We also calculate the number of pulsars predicted by our models.

Our approach is completely self-consistent: we consider the specifics of the chosen surveys to account for radio selection effects, and compare our samples with the pulsars observed by the same surveys. Figure 5 shows the mean number of predicted detections averaged over the N realizations of the radio selection effects. The FL model seems to better fit the observed pulsar distribution in the $P - \dot{P}$ plane: the predicted pulsar sample peaks at ~ 0.1 s, where the majority of pulsars lie. However, Figure 5 shows that the FL model predicts too many observed BNSs. In fact, it estimates $\sim 10^2$ observable pulsar binary systems, almost 10 times more than the number of detected Galactic BNSs. On the other hand, the FG model strongly underestimates the number of observed pulsars. The U model, instead, not only populates the $P - \dot{P}$ region where the observed pulsars lie, but also predicts the correct number of BNSs. For this reason, we choose the U model as the fiducial one. The reason why the FL model predicts a much higher number of detectable BNSs with respect to both FG and U is that it initializes the bulk of the pulsar population with lower values of both magnetic field and initial spin. Hence, more pulsars are still above the death line at current time in model FL compared to U and FG (Chattopadhyay et al. 2020).

From Figures 4 and 5, we can see another feature: the samples of detectable BNSs decrease for lower values of τ_{d} . This happens because younger pulsars constitute the great majority of the detectable pulsars. Since for lower values of τ_{d} the pulsars move faster in the $P - \dot{P}$ plane, towards larger spin periods and lower magnetic fields, pulsars cross the death line in shorter intervals of time.

Chattopadhyay et al. (2020) produce, in general, more radio selected pulsars with respect to our models, from 5 to 20 times more pulsars than our predictions (excluding their model CE-Z, which assumes no accretion during CE, as in our work, see Section 4). Nonetheless, they observe the same trend with τ_{d} .

Figure 6 shows the cumulative distributions of the orbital period, eccentricity, spin period, and spin period derivative, for our fiducial model. We show the distributions we obtained with and without accounting for the selection effects, for comparison. Radio selection effects select only the non-dead pulsars, characterized in general by smaller spin periods P and larger \dot{P} . Furthermore, binary selection effects tend to select circular with respect to eccentric systems.

In general, our models match the observed distributions, including the eccentricity distribution, when we account for selection effects.

Figure 6 also compares different CE parameters $\alpha = 0.5 - 5$. The choice of α influences the orbital period and especially the eccentricity. The models with $\alpha > 1$ better match the data with respect to those with $\alpha \leq 1$, because the latter produce too many

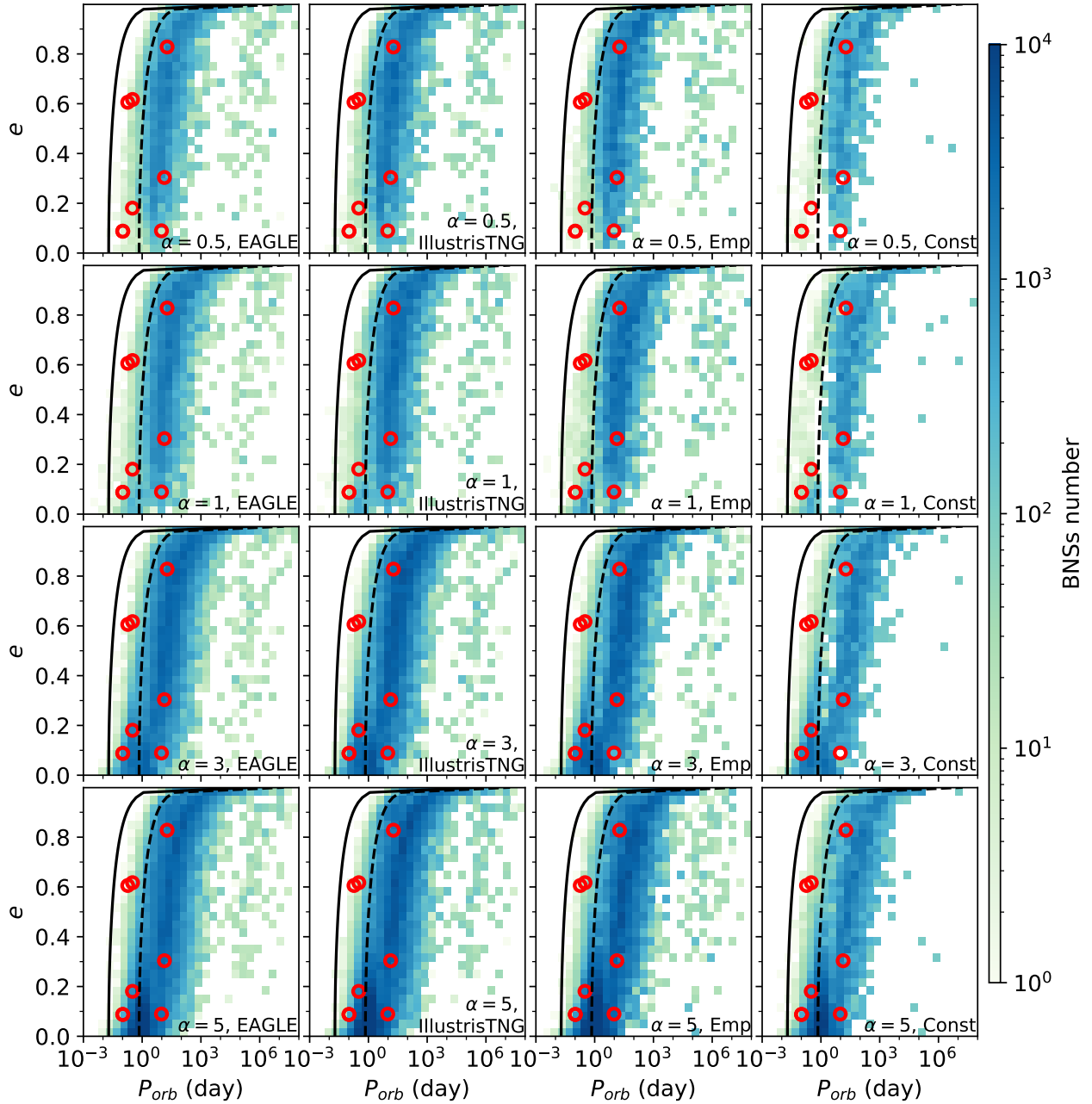


Figure 2. Distribution of the simulated BNSs at the present time in the $P_{\text{orb}} - e$ plane. Each column shows the results for a different Galaxy model, from left to right: EAGLE, ILLUSTRISTNG, Emp and Const. The rows show different α values, from top to bottom: $\alpha = 0.5$, 1, 3, and 5. All the models shown here assume $\tau_{\text{d}} = 1$ Gyr, and model U for the initial spin and magnetic field. The red circles show the observed population of BNSs selected for this study. The solid black line shows values of constant $t_{\text{GW}} = 1$ Myr, while the dashed black line corresponds to t_{GW} equal to the Hubble time. We obtained the lines of constant t_{GW} with equation D6 in [Iorio et al. \(2022\)](#)⁹, assuming a mass of $1.35 M_{\odot}$ for the NSs.

highly eccentric systems. This preference for $\alpha > 1$ when considering the eccentricity distribution points in the same direction as the result of the BNS merger rate: we found the best match with the MW merger rate for $\alpha = 3$.

The distributions of P and \dot{P} do not change much with α , as expected. The Galactic BNSs seem to have a double peaked distribution: the first peak around $P \sim 1$ d, the second one at about 10^2 d ([Andrews & Mandel 2019](#)). However, given the small sample

of detected BNSs we do not have enough statistics to claim that such feature is characteristic of the underlying BNS distribution.

⁹ The analytical methods to compute the GW merging time are implemented in the function `estimate_gw`, in the publicly available PYTHON module PYBLACK, <https://gitlab.com/iogiul/pyblack>.

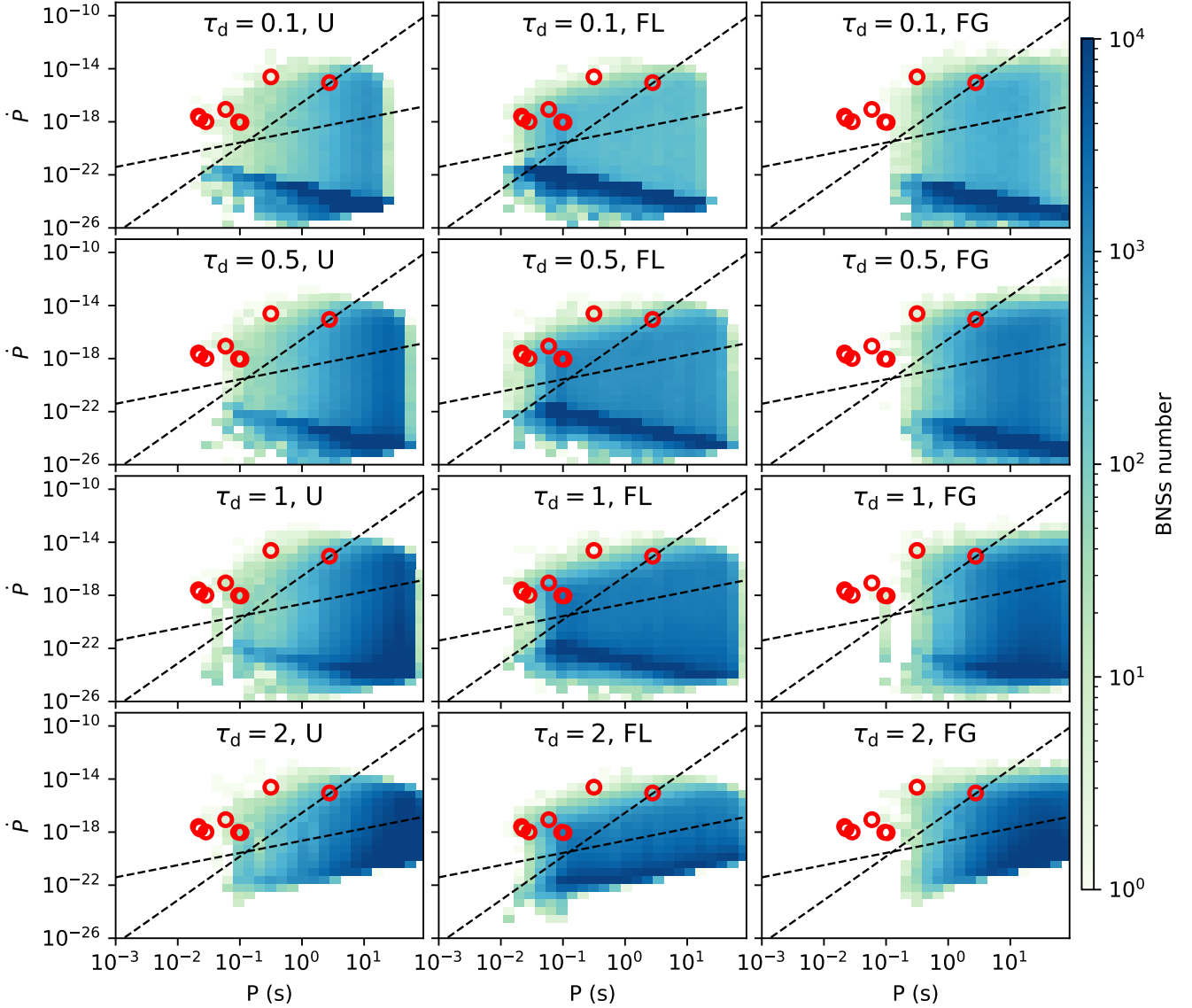


Figure 3. Distribution of the simulated BNSs at the present time in the $P - \dot{P}$ plane. Each column shows the results for a different model of the initial spin and magnetic field, from left to right: uniform (U), flat-in-log (FL), Faucher-Giguère (FG). The rows assume different values of τ_d , from left to right: $\tau_d = 0.1, 0.5, 1, 2$ Gyr. All the runs assume $\alpha = 3$ and the Emp MW model. The markers show the observed population of pulsars (Table 4). The dashed black lines show the death lines defined in Eq. 30.

3.5 Bayes factors

Table 6 shows the Bayes factors of each model, that we obtained as described in Section 2.9. For this analysis, we used four BNS parameters: orbital period, eccentricity, spin period and derivative of the spin period. Figures 7a and 7b show two examples of the DPGMMs we applied to these four parameters in our simulations.

The Bayes factors indicate that the FG distribution is strongly disfavoured in all the models, confirming what we can qualitatively see from Figures 4 and 5. Also, the U model performs better than the FL model, because the latter produces too many detectable BNSs (Fig. 5).

Considering the fiducial model, we find that $\tau_d = 1$ Gyr produces slightly better results. However, the differences yielded by distinct τ_d values are not as appreciable as those produced by different initial

spin and magnetic field distributions. Thus, we cannot confidently discard a particular value of τ_d based only on this result.

3.6 Predictions for the SKA

Within our framework, we can make predictions for the Square Kilometre Array (SKA). We applied the radio selection effects setting the parameters of the major SKA surveys (MID and LOW, see Appendix B), and studied how the predictions vary for our different models. Table 7 shows the resulting number of SKA-detectable BNSs for different models. We see a spread of about two orders of magnitude among the results. Consistently with Figure 5, the FL initial distribution predicts ~ 10 times more observable pulsars than the other models. Our fiducial model estimates that SKA will be able to observe 30 ± 6 BNSs, among which 21 ± 4 new detections.

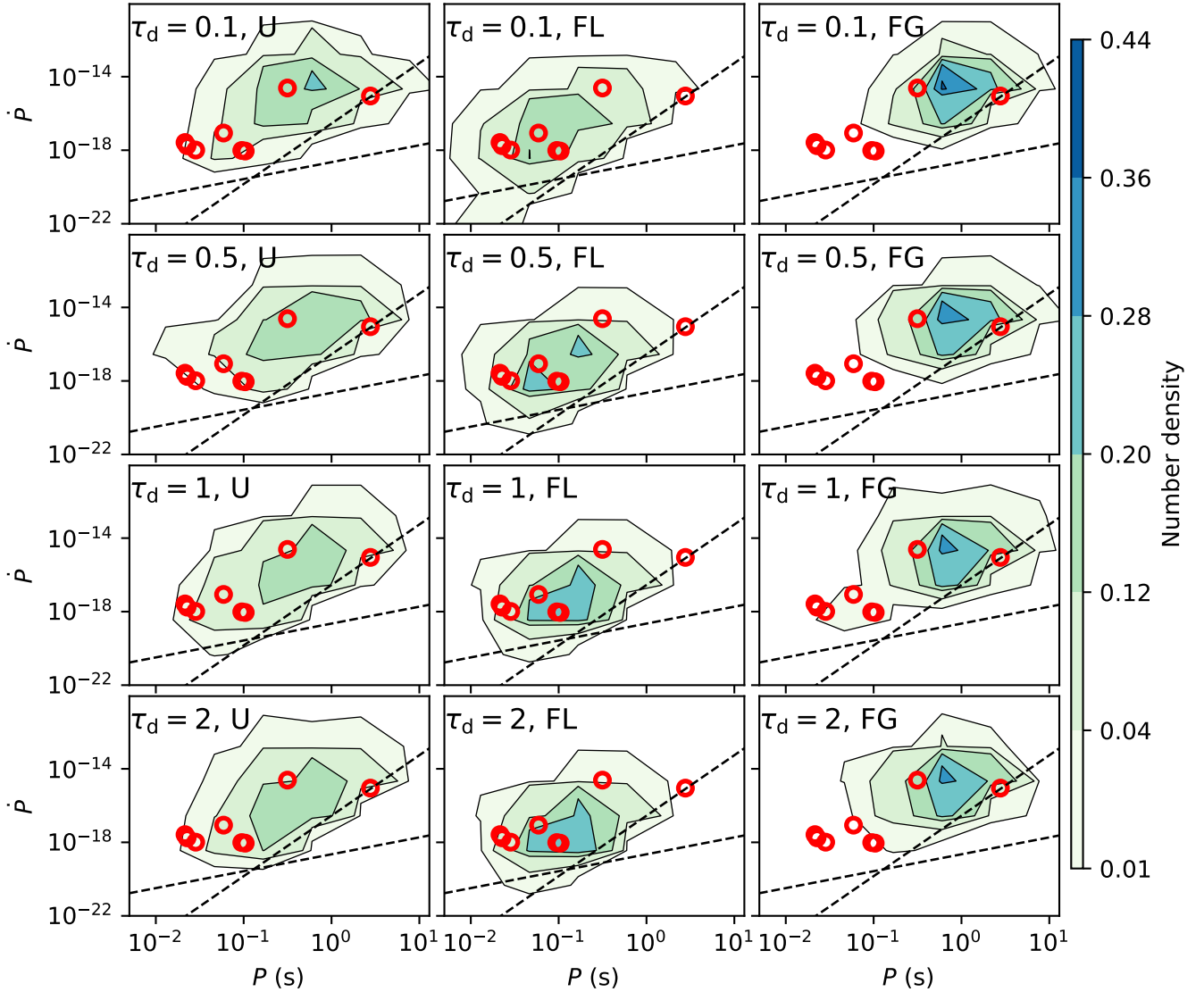


Figure 4. Isocontours showing the number density of detectable pulsars (after applying radio selection effects) in the $P - \dot{P}$ plane. Each column shows the results for a different spin and magnetic field model, from left to right: U, FL, and FG. The rows assume different values of τ_d , from left to right: $\tau_d = 0.1, 0.5, 1,$ and 2 Gyr. All the runs assume $\alpha = 3$ and the Emp model for the MW. The markers show the observed population of pulsars (Table 4). The dashed black lines show the death lines defined in Eq. 30.

α	Uniform (U)				Flat-in-log (FL)				Faucher-Giguere (FG)			
	τ_d (Gyr)				τ_d (Gyr)				τ_d (Gyr)			
	0.1	0.5	1	2	0.1	0.5	1	2	0.1	0.5	1	2
0.5	-136 (158)	-76 (99)	-129(165)	-57(65)	-9 (31)	-25 (26)	-36 (26)	-42 (26)	-148 (128)	-173 (129)	-199 (125)	-45 (28)
1	-103 (148)	-69 (85)	-71 (100)	-53(88)	-10 (28)	-23 (26)	-37 (27)	-47 (28)	-119 (128)	-96 (129)	-97 (125)	-50 (26)
3	-10 (82)	0.5 (27)	0 (29)	-0.1 (27)	-20 (23)	-65 (25)	-86 (25)	-53 (24)	-42 (62)	-27 (39)	-25 (45)	-21 (41)
5	-0.5 (27)	-55 (82)	4 (25)	-25 (27)	-27 (23)	-85 (24)	-121 (25)	-172 (26)	-37 (87)	-36 (80)	-20 (43)	-32 (46)

Table 6. Logarithmic Bayes factors ($\ln B$) of the simulated models compared to the fiducial model 'Ua3t1Emp', adopting the Emp MW model. The fiducial model is highlighted in bold face in the Table.

4 DISCUSSION

We have explored the BNS population properties within four different Galaxy models: a model with constant (Const) SFR, an empirical (Emp) MW model with exponentially decaying SFR, and two models

taken from the EAGLE and ILLUSTRITNG cosmological simulations, respectively (Table 1). In all the four models, the Galactic SFR at present day matches the one of the MW. In addition, the Emp, EAGLE, and ILLUSTRITNG models also match the current total stellar mass of the MW, whereas the Const model results in a factor of ~ 2.5

α	Uniform (U)				Flat-in-log (FL)				Faucher-Giguere (FG)			
	τ_d (Gyr)				τ_d (Gyr)				τ_d (Gyr)			
	0.1	0.5	1	2	0.1	0.5	1	2	0.1	0.5	1	2
0.5	6 (2)	10 (3)	9 (3)	11 (3)	54 (8)	121 (10)	173 (12)	211 (14)	3 (1)	5 (2)	4 (2)	210 (14)
1	9 (3)	13 (3)	10 (3)	14 (3)	84 (8)	145 (13)	196 (12)	241 (13)	6 (2)	6 (2)	7 (3)	240 (14)
3	23 (5)	29 (5)	30(6)	36 (5)	155 (12)	316 (19)	411 (18)	288 (17)	17 (4)	21 (4)	20 (4)	22 (5)
5	26 (5)	16 (4)	39 (6)	21 (5)	178 (14)	395 (20)	532 (24)	721 (29)	17 (4)	19 (4)	23 (5)	21 (5)

Table 7. Predicted number of pulsars in BNSs detectable by the SKA, after averaging over $N = 100$ realisations of the radio selection effects. We report the standard deviation on the mean within brackets. The fiducial model is highlighted in bold face in the Table.

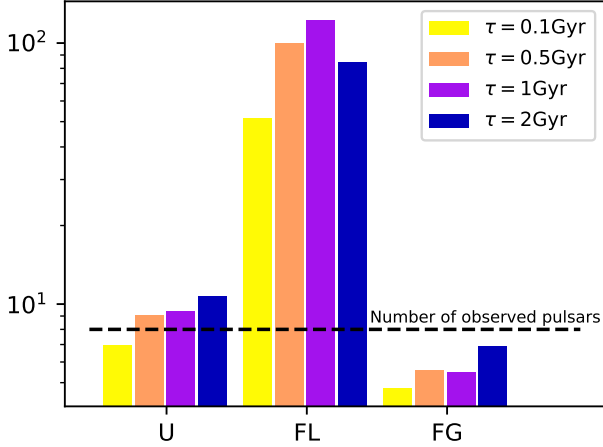


Figure 5. Mean number of radio selected pulsars predicted by our models after averaging over the $N = 100$ realizations of the selection effects, assuming the fiducial $\alpha = 3$ and the Emp MW model. Each bar is a different model: the x -axis shows the spin and magnetic field initial distributions (U, FL, and FG). Each colour is associated to a different τ_d value: yellow, pink, purple, and blue for $\tau_d = 0.1, 0.5, 1,$ and 2 Gyr, respectively. The black horizontal dashed line shows the number of observed Galactic BNSs in the considered surveys, $N_{\text{obs}} = 8$.

lower mass Galaxy. Furthermore, the SFR history of the EAGLE and ILLUSTRITNG galaxies deviate from the simple exponential decay assumed in the Emp model. The adopted models differ from each other in terms of metallicity as well: adopting the FMR, the Emp model is dominated by Solar metallicity stars, whereas the EAGLE and ILLUSTRITNG models contain a large population of metal-poor stars.

Despite these differences, the $P_{\text{orb}} - e$ distribution of BNSs in the Emp, EAGLE, and ILLUSTRITNG models show similar features. In contrast, the Const model predicts a much lower number of BNSs than the other models. This is a consequence of the lower total stellar mass of the Const model.

The Galactic BNS merger rate is primarily affected by our choice of the common-envelope parameter α . If we assume $\alpha = 3$, the resulting present-day Galactic merger rate is a factor of ~ 10 higher than for $\alpha = 0.5$, and is more consistent with the value inferred from observations (Pol et al. 2019, 2020). The merger rate is also affected by the SFR and metallicity of the adopted Galaxy model (Fig. 1).

Our models still represent a rather simplified description of the MW. Matteucci et al. (2019) and Kobayashi et al. (2023) explore detailed models of the MW, accounting also for its chemical enrichment history. They account for BNS mergers, and study if the latter can explain the r-process element abundance. Kobayashi et al. (2023) ex-

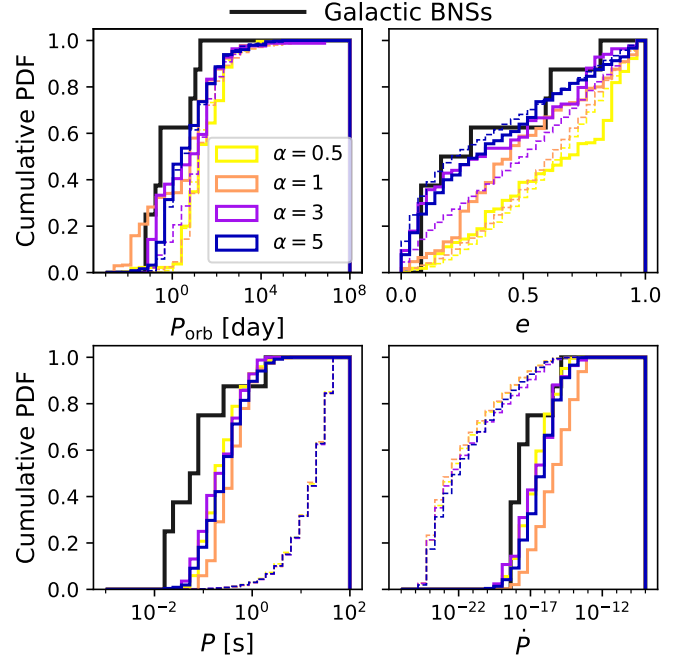


Figure 6. Cumulative distribution of the pulsar parameters P_{orb} , e , P and \dot{P} (from top left to bottom right) for the fiducial model parameters. Yellow, pink, purple, and blue solid lines: $\alpha = 0.5, 1, 3, 5$. The dashed thin lines display the underlying astrophysical BNS population, while the solid thick lines show the detectable population, after implementing radio-selection effects. The black solid line marks the cumulative distribution of the observed Galactic BNSs.

plain the relative abundances of elements through BNS mergers only with a dependence of the delay time distribution on metallicity, with lower metallicities yielding shorter delay times. Their comprehensive treatment goes beyond the purpose of this work.

Our models reproduce the orbital period and eccentricity distribution of Galactic BNSs, and match the observed BNS merger rate, in a self-consistent fashion. In particular, our fiducial model reproduces the double peak in the eccentricity distribution (Andrews & Mandel 2019): observed pulsars cluster around around $e \sim 0.1$ and $e \sim 0.6$, showing instead a gap for $0.3 \lesssim e \lesssim 0.6$. In Figure 2 ($\alpha = 3$), we can distinguish two more concentrated regions at eccentricity $e \sim 0.6$ and 0.1 . This feature becomes even more evident after the application of radio selection effects (Figure 7a). This suggests the importance of observational biases not only for the spins and magnetic fields of pulsars, but also for the orbital properties. Moreover, the distribution of pulsars in the $P_{\text{orb}} - e$ plane is almost independent of the chosen MW model, enforcing the robustness of this result.

We can compare our cumulative distributions (solid lines in Fig. 6) with the green dashed lines of Figure 6 by Chattopadhyay et al.

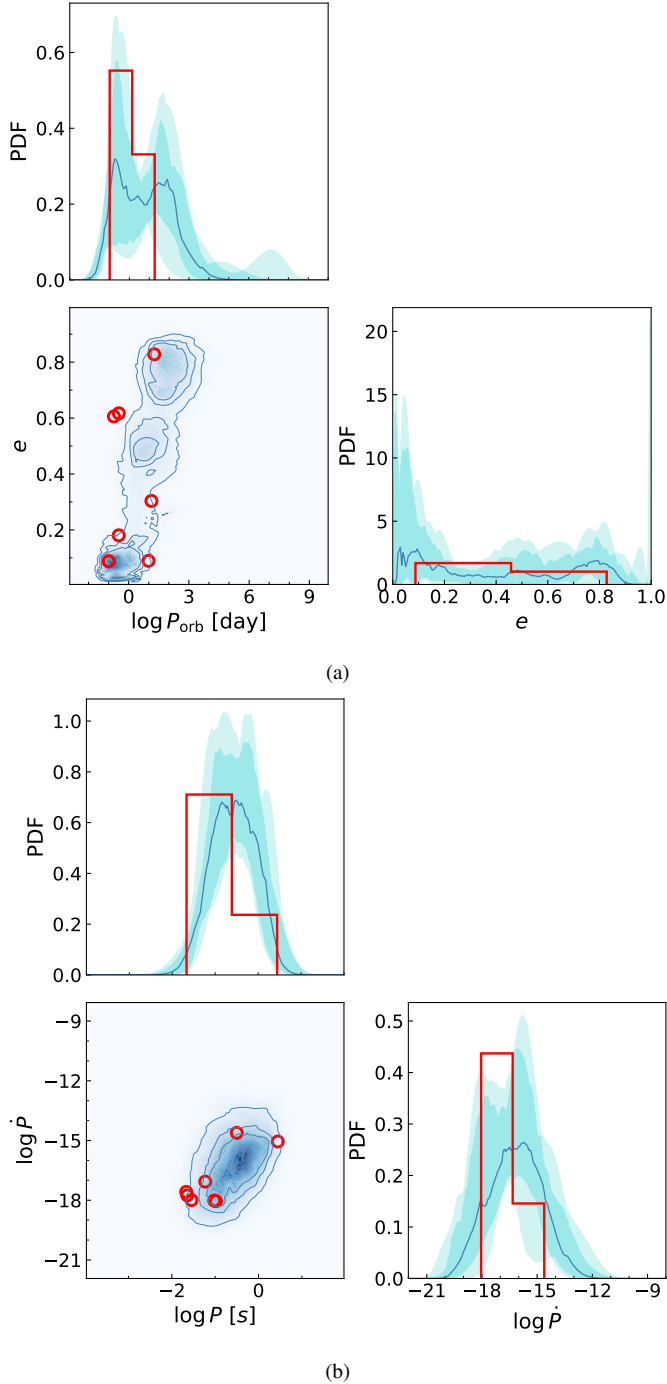


Figure 7. Two-dimensional likelihood for P_{orb} and e (panel a) and P and \dot{P} (panel b) averaged over the simulated pulsars catalogues of our fiducial model, as reconstructed by FIGARO. These likelihoods are obtained by marginalising out P and \dot{P} or P_{orb} and e from the four-dimensional likelihood, respectively. The red circles and histograms show the observed Galactic BNSs (Table 4). The blue contour lines in the 2D plot show the 90%, 68%, and 50% credible regions of the median distribution (blue lines in 1D plots). The shaded regions in 1D plots represent the 68% and 90% credible intervals for the marginal probability density for each parameter.

(2020). Our cumulative distribution of eccentricity is very different from the one reported by Chattopadhyay et al. (2020) because they do not account for binary selection effects. Our Figure 2 can be compared with those of Vigna-Gómez et al. (2018) and Kruckow et al. (2018). The distribution of BNSs in Figure 11 of Kruckow et al. (2018) is less populated at high eccentricity with respect to our results. This difference is a consequence of the different kicks and binding energy prescriptions, as discussed in Iorio et al. (2022). Compared to Kruckow et al. (2018) and our results, Vigna-Gómez et al. (2018) produce much tighter binaries (coloured dots of their Figure 2). In fact, most of the BNSs show orbital periods shorter than ~ 10 d. Moreover, the wider systems ($P_{\text{orb}} \gtrsim 10^3$ d) are completely missing. This difference is a consequence of the different natal kick models adopted in Vigna-Gómez et al. (2018).

In our models, we did not include any spin-up prescription during the CE phase. In contrast, Chattopadhyay et al. (2020) assume that a NS accretes between 0.04 and 0.1 M_{\odot} during CE, according to the rates presented in MacLeod & Ramirez-Ruiz (2015). As a result, pulsars spin up much more efficiently during a CE event than during RLO, and their distribution peaks toward smaller spin periods. For this reason, Chattopadhyay et al. (2020) predict many more detectable pulsars compared to our models when they enable accretion during CE. Nevertheless, the role played by the CE phase during spin-up is controversial (Chamandy et al. 2018). Osłowski et al. (2011) assume that the accreted matter during CE contributes only to the magnetic field decay, considering accretion during CE a chaotic process, not able to produce spin-up (Benensohn et al. 1997). Our spin-up treatment does not include the effect of winds as well. Indeed, we might expect the infalling matter produced by winds to be chaotic and thus not efficiently cause the spin-up of the pulsar (Kiel et al. 2008). We can compare Figure 5 with Table 4 from Chattopadhyay et al. (2020). The number of detectable pulsars predicted by their models is generally one order of magnitude higher than our predictions. Our predicted numbers of observable pulsars are consistent only with their model CE-Z, which does not include spin-up during CE, and predicts 13 observations.

There are large uncertainties about the surface magnetic field: the burial of magnetic field during mass accretion is poorly understood as well as its decay during the isolated pulsar evolution. The τ_d parameter has been varied in the literature from a few Myr (e.g. Osłowski et al. 2011) up to a few Gyr (e.g. Kiel et al. 2008). Another important contribution to the overall uncertainty in the pulsar population is given by the initial distribution of spins and magnetic fields. These are even more important than the magnetic-field decay time τ_d . Several distributions have been proposed for the initial spin and magnetic field (e.g. Igoshev et al. 2022; Faucher-Giguère & Kaspi 2006). However, the lack of statistics does not allow us to draw strong conclusions.

We evaluated a four-dimensional likelihood in the $(P_{\text{orb}}, e, P, \dot{P})$ space. Our approach consistently takes into account correlations among parameters, which are instead neglected by other tests (e.g., the Kolmogorov-Smirnov test), frequently used in the pulsar literature. The large errors on the Bayes factor errors reported in Table 6 are a consequence of the limited number of observed pulsars, making it difficult to differentiate among the models. However, despite this limitation, the Bayes factor indicate that the FG and FL models are disfavoured with respect to the U prescription.

We can compare our SKA predictions (Table 7) to Table 4 of Chattopadhyay et al. (2021). Their fiducial model estimates 78 BNSs containing a radio-detectable pulsar by the SKA telescope. Their result is thus roughly twice our projection. Nevertheless this discrepancy is consistent with the different approach we used. As already

stressed, the different CE formalism, accentuates the spin up of their pulsars, resulting in shorter spin periods. In turn, this translates into a higher number of detectable pulsars.

5 SUMMARY

The BNS population of the MW is the perfect laboratory to test binary-star evolution models. Here, we used the new population synthesis code *SEVN* (Iorio et al. 2022) to model the population of BNSs in the MW. We implemented a new model for both the spin down and spin up of pulsars in *SEVN*, while also probing the relevant parameter space (e.g., CE parameter α , initial spin distribution, initial magnetic field distribution, decay time of the magnetic field τ_d). We injected our simulated binaries into four MW models: an empirical model with an exponentially decaying SFR, a model with constant SFR, and two galaxies from the *EAGLE* and *ILLUSTRISTNG* cosmological simulations.

We compared our simulated BNS catalogues with the observed Galactic BNSs after applying radio selection effects with *PSRPOP* (Bates et al. 2014). In our analysis, we considered four observable parameters: orbital period, eccentricity, pulsar spin period, and spin period derivative. After modelling our radio-selected pulsars with a Dirichlet process Gaussian mixture model (Rinaldi & Del Pozzo 2022b), we evaluated the four-dimensional likelihood associated with each model in the aforementioned parameter space. We then compared our models by computing the Bayes factor with respect to the fiducial model.

We also derived the Galactic BNS merger rate from our models and compared it with the one inferred from the observations (Pol et al. 2019, 2020). The CE parameter α has a large impact on both the merger rate and the orbital properties of the BNS population. The present-day BNS merger rate varies up to one order of magnitude depending on the choice of α . Values of $\alpha < 1$ are disfavoured as they under-predict the merger rates and produce more eccentric systems compared to observations (Fig. 6). Assuming the empirical MW prescription, the model with $\alpha = 3$ produces a rate $\mathcal{R}_{\text{MW}} = 31.3 \text{ Myr}^{-1}$ (Fig. 1), consistent with the rate inferred from the Galactic pulsar binary systems ($\mathcal{R}_{\text{MW}} = 37_{-11}^{+24} \text{ Myr}^{-1}$, Pol et al. 2020).

The distribution of magnetic field and spin period at pulsar formation play a critical role on the final population of detectable pulsars (Fig. 4). The Bayes factors favour the uniform (U) distribution of spin periods and magnetic fields, which predicts 5–10 detectable pulsars. In contrast, the flat-in-log (FL) model predicts ~ 100 detectable pulsars (Fig. 5) against the 8 observed Galactic pulsars in the considered surveys (the Parkes Multibeam Pulsar Survey, the Swinburne Multibeam Pulsar Survey, and the High Time Resolution Universe Pulsar Survey).

The magnetic field decay timescale τ_d is another free parameter of our model. There are large uncertainties on the physical process leading to the burial of the magnetic field and consequently to the typical timescales associated with it. τ_d dictates the speed at which a pulsar traverses the $P - \dot{P}$ plane and stops emitting radio beams. Given the small sample of Galactic BNSs, we cannot draw strong conclusions on the expected τ_d value.

We have shown that we need to account for radio selection effects in order to reproduce the observed spin period and magnetic field distributions of observed pulsars. Moreover, binary selection effects are critical to correctly match the orbital period and especially the eccentricity distribution of the observed Galactic BNSs.

According to our fiducial model, which matches both the Galactic merger rate and the orbital properties of Galactic BNSs, the SKA

will observe ~ 30 BNSs in the Milky Way, among which ~ 20 new detections.

ACKNOWLEDGEMENTS

We thank Hurley et al. (2002) for making the BSE code publicly available. MM and GI acknowledge financial support from the European Research Council for the ERC Consolidator grant DEMOBLACK, under contract no. 770017. MM acknowledges support from PRIN-MIUR 2020 METE, under contract no. 2020KB33TP. This work has been funded using resources from the INAF Large Grant 2022 ‘‘GC-jewels’’ (P.I. Andrea Possenti) approved with the Presidential Decree 30/2022. MCA acknowledges financial support from the Seal of Excellence @UNIPD 2020 program under the ACROGAL project. MS acknowledges financial support from the National Research Centre for High Performance Computing, Big Data and Quantum Computing (ICSC), and from the program ‘‘Data Science methods for Multi-Messenger Astrophysics & Multi-Survey Cosmology’’ funded by the Italian Ministry of University and Research, Programmazione triennale 2021/2023 (DM n.2503 dd. 09/12/2019), Programma Congiunto Scuole. This research made use of NUMPY (Harris et al. 2020), SCIPY (Virtanen et al. 2020). For the plots we used MATPLOTLIB (Hunter 2007). To model the radio selection effects we used PSRPOP (Bates et al. 2014).

DATA AVAILABILITY

This work made use of the codes *SEVN* (Iorio et al. 2022) available at the gitlab repository <https://gitlab.com/sevncodes/sevn> (release *Sgalletta23*, <https://gitlab.com/sevncodes/sevn/-/releases/sgalletta23>), and *FIGARO*, presented in Rinaldi & Del Pozzo (2022b). The list of *SEVN* parameters used in this work can be found at the following link: <https://doi.org/10.5281/zenodo.7887279> (Sgalletta et al. 2023). Further data will be shared based on reasonable request to the corresponding authors.

REFERENCES

- Abbott B. P., et al., 2017a, *Phys. Rev. Lett.*, 119, 161101
 Abbott B. P., et al., 2017b, *ApJ*, 848, L12
 Abbott B. P., et al., 2018, *Phys. Rev. Lett.*, 121, 161101
 Abbott B. P., et al., 2020, *ApJ*, 892, L3
 Ade P. A. R., et al., 2014, *A&A*, 571, A16
 Ade P. A. R., et al., 2016, *A&A*, 594, A13
 Andersen B. C., Ransom S. M., 2018, *ApJ*, 863, L13
 Andrews J. J., Mandel I., 2019, *ApJ*, 880, L8
 Artale M. C., Mapelli M., Giacobbo N., Sabha N. B., Spera M., Santoliquido F., Bressan A., 2019, *MNRAS*, 487, 1675
 Artale M. C., Mapelli M., Bouffanais Y., Giacobbo N., Pasquato M., Spera M., 2020a, *MNRAS*, 491, 3419
 Artale M. C., Bouffanais Y., Mapelli M., Giacobbo N., Sabha N. B., Santoliquido F., Pasquato M., Spera M., 2020b, *MNRAS*, 495, 1841
 Arzoumanian Z., et al., 2018, *ApJS*, 235, 37
 Arzoumanian Z., et al., 2020, *ApJ*, 905, L34
 Asplund M., Grevesse N., Sauval A. J., Scott P., 2009, *ARA&A*, 47, 481
 Bagchi M., Lorimer D., Wolfe S., 2013, *Monthly Notices of the Royal Astronomical Society*, 432
 Balakrishnan V., Champion D., Barr E., Kramer M., Venkatraman Krishnan V., Eatough R. P., Sengar R., Bailes M., 2022, *MNRAS*, 511, 1265
 Bates S. D., Lorimer D. R., Rane A., Swiggum J., 2014, *MNRAS*, 439, 2893
 Bauswein A., Just O., Janka H.-T., Stergioulas N., 2017, *ApJ*, 850, L34
 Belczynski K., et al., 2018, *A&A*, 615, A91

- Belczynski K., et al., 2020, *A&A*, **636**, A104
- Benensohn J. S., Lamb D. Q., Taam R. E., 1997, *ApJ*, **478**, 723
- Bhat N. D. R., Cordes J. M., Camilo F., Nice D. J., Lorimer D. R., 2004, *ApJ*, **605**, 759
- Bhattacharya D., Wijers R. A. M. J., Hartman J. W., Verbunt F., 1992, *A&A*, **254**, 198
- Blaauw A., 1961, *Bull. Astron. Inst. Netherlands*, **15**, 265
- Boco L., Lapi A., Goswami S., Perrotta F., Baccigalupi C., Danese L., 2019, *ApJ*, **881**, 157
- Boco L., Lapi A., Chruslinska M., Donevski D., Sicilia A., Danese L., 2021, *ApJ*, **907**, 110
- Bogdanov S., Heinke C. O., Özel F., Güver T., 2016, *ApJ*, **831**, 184
- Bouffanais Y., Mapelli M., Santoliquido F., Giacobbo N., Iorio G., Costa G., 2021, *Monthly Notices of the Royal Astronomical Society*, **505**, 3873
- Bovy J., 2017, *MNRAS*, **470**, 1360
- Bray J. C., Eldridge J. J., 2016, *MNRAS*, **461**, 3747
- Bray J. C., Eldridge J. J., 2018, *MNRAS*, **480**, 5657
- Bressan A., Marigo P., Girardi L., Salasnich B., Dal Cero C., Rubele S., Nanni A., 2012, *MNRAS*, **427**, 127
- Breton R. P., et al., 2008, *Science*, **321**, 104
- Broekgaarden F. S., et al., 2021, *MNRAS*, **508**, 5028
- Broekgaarden F. S., et al., 2022, *MNRAS*, **516**, 5737
- Brown G. E., 1995, *ApJ*, **440**, 270
- Burgay M., et al., 2003, *Nature*, **426**, 531
- Cameron A. D., et al., 2018, *MNRAS*, **475**, L57
- Chamandy L., et al., 2018, *Monthly Notices of the Royal Astronomical Society*, **480**, 1898
- Chattopadhyay D., Stevenson S., Hurley J. R., Rossi L. J., Flynn C., 2020, *MNRAS*, **494**, 1587
- Chattopadhyay D., Stevenson S., Hurley J. R., Bailes M., Broekgaarden F., 2021, *MNRAS*, **504**, 3682
- Chiappini C., Matteucci F., Gratton R., 1997, *ApJ*, **477**, 765
- Chruslinska M., Belczynski K., Kléncki J., Benacquista M., 2018, *MNRAS*, **474**, 2937
- Chruslinska M., Nelemans G., Boco L., Lapi A., 2021, *MNRAS*, **508**, 4994
- Claeys J. S. W., Pols O. R., Izzard R. G., Vink J., Verbunt F. W. M., 2014, *A&A*, **563**, A83
- Colombo A., Salafia O. S., Gabrielli F., Ghirlanda G., Giacomazzo B., Perego A., Colpi M., 2022, *ApJ*, **937**, 79
- Combi L., Siegel D. M., 2023, *ApJ*, **944**, 28
- Cordes J. M., 2004, in Clemens D., Shah R., Brainerd T., eds, *Astronomical Society of the Pacific Conference Series Vol. 317, Milky Way Surveys: The Structure and Evolution of our Galaxy*. p. 211
- Cordes J. M., Lazio T. J. W., 2002, arXiv e-prints, [pp astro-ph/0207156](https://arxiv.org/abs/pp astro-ph/0207156)
- Corongiu A., Kramer M., Stappers B. W., Lyne A. G., Jessner A., Possenti A., D'Amico N., Löhmer O., 2007, *A&A*, **462**, 703
- Costa G., Girardi L., Bressan A., Marigo P., Rodrigues T. S., Chen Y., Lanza A., Goudfrooij P., 2019, *Monthly Notices of the Royal Astronomical Society*, **485**, 4641
- Costa G., Bressan A., Mapelli M., Marigo P., Iorio G., Spera M., 2021, *MNRAS*, **501**, 4514
- Côté B., et al., 2019, *ApJ*, **875**, 106
- Courteau S., et al., 2014, *Reviews of Modern Physics*, **86**, 47
- Dewey R. J., Taylor J. H., Weisberg J. M., Stokes G. H., 1985, *ApJ*, **294**, L25
- Dewi J. D. M., Podsiadlowski P., Sena A., 2006, *MNRAS*, **368**, 1742
- Di Stefano R., Kruckow M. U., Gao Y., Neunteufel P. G., Kobayashi C., 2023, *ApJ*, **944**, 87
- Edwards R. T., Bailes M., van Straten W., Britton M. C., 2001, *MNRAS*, **326**, 358
- Eggleton P. P., 1983, *ApJ*, **268**, 368
- Eichler D., Livio M., Piran T., Schramm D. N., 1989, *Nature*, **340**, 126
- Faucher-Giguère C.-A., Kaspi V. M., 2006, *ApJ*, **643**, 332
- Faulkner A. J., et al., 2004, *MNRAS*, **355**, 147
- Fragos T., Andrews J. J., Ramirez-Ruiz E., Meynet G., Kalogera V., Taam R. E., Zezas A., 2019, *ApJ*, **883**, L45
- Fryer C. L., Belczynski K., Wiktorowicz G., Dominik M., Kalogera V., Holz D. E., 2012, *ApJ*, **749**, 91
- Fujibayashi S., Kiuchi K., Wanajo S., Kyutoku K., Sekiguchi Y., Shibata M., 2023, *ApJ*, **942**, 39
- Gessner A., Janka H.-T., 2018, *ApJ*, **865**, 61
- Giacobbo N., Mapelli M., 2018, *MNRAS*, **480**, 2011
- Giacobbo N., Mapelli M., 2019, *MNRAS*, **482**, 2234
- Giacobbo N., Mapelli M., 2020, *ApJ*, **891**, 141
- Giacobbo N., Mapelli M., Spera M., 2018, *MNRAS*, **474**, 2959
- Goldreich P., Julian W. H., 1969, *ApJ*, **157**, 869
- Goldreich P., Reisenegger A., 1992, *ApJ*, **395**, 250
- Goldstein A., et al., 2017, *ApJ*, **848**, L14
- Gonthier P. L., Van Guilder R., Harding A. K., 2004, *ApJ*, **604**, 775
- Grisoni V., Spitoni E., Matteucci F., Recio-Blanco A., de Laverny P., Hayden M., Mikolaitis Š., Worley C. C., 2017, *MNRAS*, **472**, 3637
- Harris C. R., et al., 2020, *Nature*, **585**, 357
- Haslam C. G. T., Klein U., Salter C. J., Stoffel H., Wilson W. E., Cleary M. N., Cooke D. J., Thomasson P., 1981, *A&A*, **100**, 209
- Hewish A., Bell S. J., Pilkington J. D. H., Scott P. F., Collins R. A., 1968, *Nature*, **217**, 709
- Hirai R., Mandel I., 2022, *ApJ*, **937**, L42
- Hobbs G., 2013, *Classical and Quantum Gravity*, **30**, 224007
- Hobbs G., Lorimer D. R., Lyne A. G., Kramer M., 2005, *Monthly Notices of the Royal Astronomical Society*, **360**, 974
- Hobbs G., et al., 2010, *Classical and Quantum Gravity*, **27**, 084013
- Hotkezaka K., Beniamini P., Piran T., 2018, *International Journal of Modern Physics D*, **27**, 1842005
- Hulse R. A., Taylor J. H., 1975, *ApJ*, **195**, L51
- Hunt L., Dayal P., Magrini L., Ferrara A., 2016, *MNRAS*, **463**, 2020
- Hunter J. D., 2007, *Computing in Science and Engineering*, **9**, 90
- Hurley J. R., Tout C. A., Pols O. R., 2002, *MNRAS*, **329**, 897
- Igoshev A. P., Frantsuzova A., Gourgouliatos K. N., Tsihli S., Konstantinou L., Popov S. B., 2022, *MNRAS*, **514**, 4606
- Illarionov A. F., Sunyaev R. A., 1975, *A&A*, **39**, 185
- Iorio G., et al., 2022, arXiv e-prints, [p. arXiv:2211.11774](https://arxiv.org/abs/p. arXiv:2211.11774)
- Ivanova N., et al., 2013, *A&ARv*, **21**, 59
- Janka H. T., Mueller E., 1994, *A&A*, **290**, 496
- Justham S., Podsiadlowski P., Han Z., 2011, *MNRAS*, **410**, 984
- Kapil V., Mandel I., Berti E., Müller B., 2023, *MNRAS*, **519**, 5893
- Kasen D., Metzger B., Barnes J., Quataert E., Ramirez-Ruiz E., 2017, *Nature*, **551**, 80
- Kaspi V. M., Taylor J. H., Ryba M. F., 1994, *ApJ*, **428**, 713
- Keith M. J., Eatough R. P., Lyne A. G., Kramer M., Possenti A., Camilo F., Manchester R. N., 2009, *MNRAS*, **395**, 837
- Keith M. J., et al., 2010, *MNRAS*, **409**, 619
- Kiel P. D., Hurley J. R., Bailes M., Murray J. R., 2008, *Monthly Notices of the Royal Astronomical Society*, **388**, 393
- Kléncki J., Nelemans G., Istrate A. G., Chruslinska M., 2021, *A&A*, **645**, A54
- Kobayashi C., et al., 2023, *ApJ*, **943**, L12
- Konar S., Bhattacharya D., 1997, *Monthly Notices of the Royal Astronomical Society*, **284**, 311
- Konar S., Bhattacharya D., 1999, *Monthly Notices of the Royal Astronomical Society*, **303**, 588
- Kramer M., et al., 2006, *Science*, **314**, 97
- Kramer M., et al., 2021, *Physical Review X*, **11**, 041050
- Kroupa P., 2001, *MNRAS*, **322**, 231
- Kruckow M. U., Tauris T. M., Langer N., Kramer M., Izzard R. G., 2018, *MNRAS*, **481**, 1908
- Lai D., Chernoff D. F., Cordes J. M., 2001, *ApJ*, **549**, 1111
- Lattimer J. M., 2021, *Annual Review of Nuclear and Particle Science*, **71**, 433
- Lentati L., et al., 2015, *MNRAS*, **453**, 2576
- Licquia T. C., Newman J. A., 2015, *ApJ*, **806**, 96
- Lorimer D. R., 2008, *Living Reviews in Relativity*, **11**, 8
- Lorimer D., 2011, *Astrophysics Source Code Library*, pp 07019–
- Lorimer D. R., Kramer M., 2004, *Handbook of Pulsar Astronomy*. Vol. 4
- Lyne A. G., Manchester R. N., 1988, *MNRAS*, **234**, 477
- Lyne A. G., et al., 2004, *Science*, **303**, 1153

- Lyne A., Hobbs G., Kramer M., Stairs I., Stappers B., 2010, *Science*, **329**, 408
- MacLeod M., Ramirez-Ruiz E., 2015, *ApJ*, **803**, 41
- Manchester R. N., et al., 2001, *MNRAS*, **328**, 17
- Manchester R. N., Hobbs G. B., Teoh A., Hobbs M., 2005, *AJ*, **129**, 1993
- Manchester R. N., et al., 2013, *Publ. Astron. Soc. Australia*, **30**, e017
- Mandel I., Broekgaarden F. S., 2022, *Living Reviews in Relativity*, **25**, 1
- Mannucci F., Cresci G., Maiolino R., Marconi A., Gnerucci A., 2010, *MNRAS*, **408**, 2115
- Mannucci F., Salvaterra R., Campisi M. A., 2011, *MNRAS*, **414**, 1263
- Mapelli M., Giacobbo N., 2018, *MNRAS*, **479**, 4391
- Mapelli M., Giacobbo N., Ripamonti E., Spera M., 2017, *MNRAS*, **472**, 2422
- Mapelli M., Giacobbo N., Santoliquido F., Artale M. C., 2019, *MNRAS*, **487**, 2
- Mapelli M., Spera M., Montanari E., Limongi M., Chieffi A., Giacobbo N., Bressan A., Bouffanais Y., 2020, *ApJ*, **888**, 76
- Martinez J. G., et al., 2015, *ApJ*, **812**, 143
- Matteucci F., Romano D., Cescutti G., Simonetti P., 2019, *Rendiconti Lincei. Scienze Fisiche e Naturali*, **30**, 85
- McMillan P. J., 2017, *MNRAS*, **465**, 76
- Metzger B. D., 2017, *Living Reviews in Relativity*, **20**, 3
- Metzger B. D., 2019, *Living Reviews in Relativity*, **23**, 1
- Miles M. T., et al., 2023, *MNRAS*, **519**, 3976
- Müller B., et al., 2019, *MNRAS*, **484**, 3307
- Murase K., et al., 2018, *ApJ*, **854**, 60
- Nedora V., Dietrich T., Shibata M., Pohl M., Crosato Menegazzi L., 2023, *MNRAS*, **520**, 2727
- Neijssel C. J., et al., 2019, *MNRAS*, **490**, 3740
- Nelemans G., Verbunt F., Yungelson L. R., Portegies Zwart S. F., 2000, *A&A*, **360**, 1011
- Nelson D., et al., 2019a, *Computational Astrophysics and Cosmology*, **6**, 2
- Nelson D., et al., 2019b, *MNRAS*, **490**, 3234
- Ng C., et al., 2015, *MNRAS*, **450**, 2922
- Ng C., et al., 2018, *MNRAS*, **476**, 4315
- Nguyen C. T., et al., 2022, *A&A*, **665**, A126
- O'Doherty T. N., Bahramian A., Miller-Jones J. C. A., Goodwin A. J., Mandel I., Willcox R., Atri P., Strader J., 2023, *MNRAS*, **521**, 2504
- Olejak A., Belczynski K., Ivanova N., 2021, *A&A*, **651**, A100
- Olejak A., Fryer C. L., Belczynski K., Baibhav V., 2022, *MNRAS*, **516**, 2252
- Ośłowski S., Bulik T., Gondek-Rosińska D., Belczyński K., 2011, *MNRAS*, **413**, 461
- Ostriker J. P., Gunn J. E., 1969, *ApJ*, **157**, 1395
- Özel F., Psaltis D., Narayan R., Santos Villarreal A., 2012, *ApJ*, **757**, 55
- Özel F., Psaltis D., Güver T., Baym G., Heinke C., Guillot S., 2016, *ApJ*, **820**, 28
- Pacini F., 1968, *Nature*, **219**, 145
- Paczynski B., 1976, in Eggleton P., Mitton S., Whelan J., eds, *Structure and Evolution of Close Binary Systems*. p. 75
- Perna R., Artale M. C., Wang Y.-H., Mapelli M., Lazzati D., Sgalletta C., Santoliquido F., 2022, *MNRAS*, **512**, 2654
- Peters P. C., 1964, *Phys. Rev.*, **136**, B1224
- Pezzuoli G., Fraternali F., 2015, *Monthly Notices of the Royal Astronomical Society*, **455**, 2308
- Pillepich A., et al., 2019, *MNRAS*, **490**, 3196
- Pillepich A., et al., 2023, *arXiv e-prints*, p. arXiv:2303.16217
- Pol N., McLaughlin M., Lorimer D. R., 2019, *ApJ*, **870**, 71
- Pol N., McLaughlin M., Lorimer D. R., 2020, *Research Notes of the American Astronomical Society*, **4**, 22
- Radice D., Bernuzzi S., Perego A., 2020, *Annual Review of Nuclear and Particle Science*, **70**, 95
- Riley J., et al., 2022, *ApJS*, **258**, 34
- Rinaldi S., Del Pozzo W., 2022a, *MNRAS*, **509**, 5454
- Rinaldi S., Del Pozzo W., 2022b, *MNRAS*, **517**, L5
- Roepke F. K., De Marco O., 2022, *arXiv e-prints*, p. arXiv:2212.07308
- Rudak B., Ritter H., 1994, *Monthly Notices of the Royal Astronomical Society*, **267**, 513
- Sana H., et al., 2012, *Science*, **337**, 444
- Santoliquido F., Mapelli M., Artale M. C., Boco L., 2022, *Monthly Notices of the Royal Astronomical Society*, **516**, 3297
- Schaye J., et al., 2014, *Monthly Notices of the Royal Astronomical Society*, **446**, 521
- Sgalletta C., et al., 2023, SEVN parameter file from the paper "Binary neutron star populations in the Milky Way" by Sgalletta et al., 2023, doi:10.5281/zenodo.7887279, <https://doi.org/10.5281/zenodo.7887279>
- Shao Y., Li X.-D., 2018, *ApJ*, **867**, 124
- Smartt S. J., et al., 2017, *Nature*, **551**, 75
- Spera M., Mapelli M., 2017, *MNRAS*, **470**, 4739
- Spera M., Mapelli M., Giacobbo N., Trani A. A., Bressan A., Costa G., 2019, *MNRAS*, **485**, 889
- Spera M., Trani A. A., Mencagli M., 2022, *Galaxies*, **10**, 76
- Springel V., 2005, *MNRAS*, **364**, 1105
- Springel V., 2010, *MNRAS*, **401**, 791
- Stairs I. H., Thorsett S. E., Taylor J. H., Wolszczan A., 2002, *ApJ*, **581**, 501
- Stappers B. W., Keane E. F., Kramer M., Possenti A., Stairs I. H., 2018, *Philosophical Transactions of the Royal Society of London Series A*, **376**, 20170293
- Stevenson S., Willcox R., Vigna-Gómez A., Broekgaarden F., 2022, *MNRAS*, **513**, 6105
- Szary A., Zhang B., Melikidze G. I., Gil J., Xu R.-X., 2014, *ApJ*, **784**, 59
- Tanvir N. R., Levan A. J., Fruchter A. S., Hjorth J., Hounsell R. A., Wiersema K., Tunnicliffe R. L., 2013, *Nature*, **500**, 547
- Tauris T. M., Manchester R. N., 1998, *Monthly Notices of the Royal Astronomical Society*, **298**, 625
- Tauris T. M., Langer N., Podsiadlowski P., 2015, *MNRAS*, **451**, 2123
- Tauris T. M., et al., 2017, *ApJ*, **846**, 170
- The EAGLE team 2017, *arXiv e-prints*, p. arXiv:1706.09899
- Thrane E., Osłowski S., Lasky P. D., 2020, *MNRAS*, **493**, 5408
- Tout C. A., Aarseth S. J., Pols O. R., Eggleton P. P., 1997, *MNRAS*, **291**, 732
- Troja E., et al., 2017, *Nature*, **551**, 71
- Urpin V., Konenkov D., 1997, *Monthly Notices of the Royal Astronomical Society*, **292**, 167
- Vigna-Gómez A., et al., 2018, *MNRAS*, **481**, 4009
- Vigna-Gómez A., et al., 2020, *Publ. Astron. Soc. Australia*, **37**, e038
- Virtanen P., et al., 2020, *Nature Methods*, **17**, 261
- Webbink R. F., 1985, in Pringle J. E., Wade R. A., eds, *Interacting Binary Stars*. p. 39
- Weisberg J. M., Huang Y., 2016, *ApJ*, **829**, 55
- Woosley S. E., 1987, in Helfand D. J., Huang J. H., eds, *Vol. 125, The Origin and Evolution of Neutron Stars*. p. 255
- Yusifov I., Küçük I., 2004, *A&A*, **422**, 545
- Zhang C. M., Kojima Y., 2006, *MNRAS*, **366**, 137

APPENDIX A: MASSES

Figure A1 shows the BNS masses we obtained for the three core-collapse SN models we assumed (Section 2.1). The distributions computed with the rapid and delayed models by Fryer et al. (2012) produce a strong peak of the secondary mass at about $1.2M_{\odot}$, failing to reproduce the observed masses of the Galactic BNSs. In contrast, the rapid-gauss model matches the observed population by construction. We decided to exclude the masses from the statistical analysis in Section 3.5 because the only models that matches the observation does it by construction.

APPENDIX B: SKA SURVEY PARAMETERS

Table B1 shows the SKA survey parameters in the MID- and LOW-frequency ranges (Stappers et al. 2018) we used to obtain Table 7.

This paper has been typeset from a $\text{\TeX}/\text{\LaTeX}$ file prepared by the author.

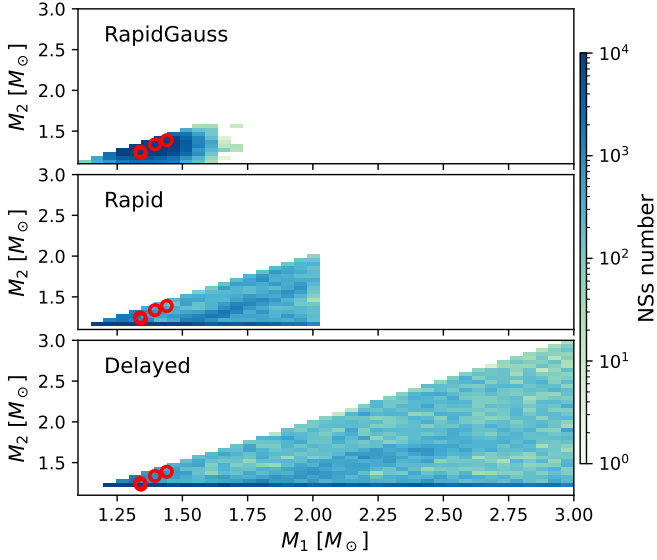


Figure A1. Secondary versus primary mass of the simulated BNSs, for the three different SN prescriptions adopted in this work. From top to bottom: rapid-gauss, rapid, and delayed. Here, the primary (secondary) is the most (least) massive NS of each BNS. The colour shows the number of binaries in each cell. The red circles are the observed Galactic BNS masses (some of the circles overlap in this Figure).

Survey	$\Delta\nu$ (MHz)	G_A (K/Jy)	T_{rec} (K)	τ_{samp} (ms)	t_{int} (s)	Sky coverage
LOW	100	26.85	56	0.1	600	$-90^\circ < \delta < 30^\circ$
MID	300	3.92	20	0.1	600	$-90^\circ < \delta < 30^\circ$

Table B1. Adopted parameters for the LOW and MID SKA surveys (Stappers et al. 2018). The columns show the bandwidth $\Delta\nu$, the antenna gain G_A , the system temperature T_{rec} , the sampling time τ_{samp} , the integration time t_{int} and the sky coverages, respectively.